J. Fluid Mech. (1993), *vol.* 247, *pp.* 339–368

The growth of large scales at defect sites in the plane mixing layer

By T. DALLARD AND F. K. BROWAND

Department of Aerospace Engineering, University of Southern California, Los Angeles, CA 90089-1191, USA

(Received 14 August 1991 and in revised form 2 September 1992)

The evolution of vortex structure in the vicinity of a pattern defect or dislocation, generated experimentally by forcing a high Reynolds number mixing layer, is studied using a new two-dimensional wavelet transform called *Arc*. This transform localizes spectral information in physical space – as all wavelets do – but is not direction-specific in wavenumber space. Various types of forcing, including forcing at the fundamental and subharmonic wavenumbers, produce a range of mixing-layer responses. The most significant finding is that a dislocation site acts as a nucleus and initiates a rapid, localized evolution to larger scales. The area of the localized 'patch' grows approximately as the square of downstream distance. Defect-initiated patches bear generic similarities to the disturbed regions in cylinder wakes – commented upon recently by many researchers – and in particular to the Λ-structures described by Williamson (1992).

1. Motivation for the present study

1.1. *Earlier work on vortex patterns*

A typical high Reynolds number free shear flow of technological interest may contain four or more decades of scales. The smaller scales – the inertial subrange and beyond – may develop a measure of independence from the particular geometry in which they arise. But larger scales remain constantly in contact with the external boundaries of the flow: these scales define the global geometry of the turbulent zone. Such flows often possess a homogeneous direction in which neither boundary conditions nor stream properties vary. There is a strong tendency for the large-scale structure to reflect this independence, but, of course, not perfectly. How these largest features exhibit three-dimensionality is the subject of the present study.

In an earlier paper, Browand & Troutt (1980) determined the correlation between velocity probes separated along the span. As the flow proceeded downstream, the physical separation required to achieve a fixed level of correlation first decreased by about a factor of three. Beyond a downstream position of 6–8 unstable wavelengths, the separation length began to increase as a linear function of distance. This linear increase in the lateral scale is not surprising. The simplest turbulent scaling requires linear growth for the largest scales not directly influenced by viscosity. The geometric structure which gives rise to the result consists of concentrations of vorticity (simply vortices), which are long compared to the correlation scale. In this linear growth region, it was observed that the vortices become distorted and intertwined over a portion of their spanwise extent. That is, vortex pairing is a three-dimensional process. At any moment, typical vortices have paired only over a

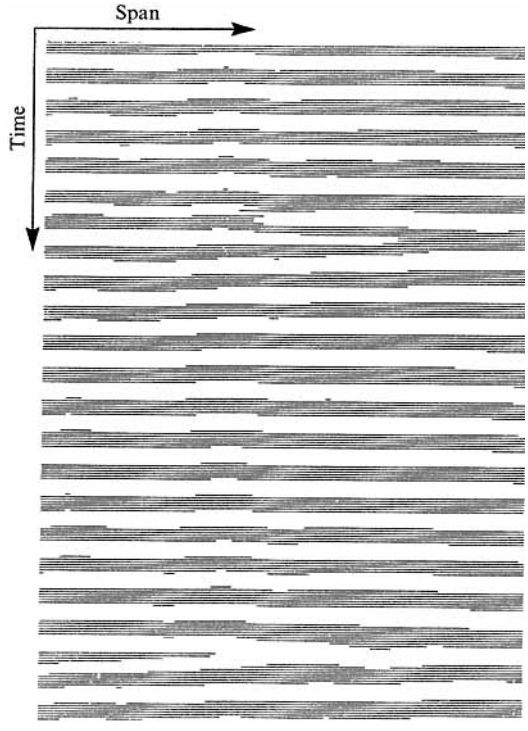

FIGURE 1. Pattern defect in the instability wave field with no forcing. The display is a two-level contour plot of the velocity fluctuation u' at 1.2 wavelengths downstream. Eleven simultaneous measurements are made across span at a vertical position $+0.4\delta$ above the flow centreplane.

portion of their spanwise length. The result is an overall structure consisting of a continuous progression of Y-branched vortices (Browand 1986; Browand & Ho 1987). This state was described as helical pairing by Chandrsuda *et al.* (1978), and was given additional support by the stability study of Pierrehumbert & Widnall (1982), and the numerical studies of Corcos & Lin (1984).

The origin of the branching in the first few wavelengths has been explored more recently by Browand & Prost-Domasky (1990). It was discovered that branching arises very early in the process of natural transition, and long before any pairing takes place. (Natural transition is taken to mean that no overt excitation has been imposed, so that transition arises as a result of the broadband, low-amplitude disturbances always present in experiments.) At a distance of 1.2 instability wavelengths downstream, features described as pattern defects had already appeared in the vortex structure. (Signal levels at this point were only a few percent of the free-stream velocity, and no measurements could be made closer to the plate trailing edge.) A typical measurement is shown in figure 1, which maps wave crests of the disturbance field as a function of span and time. It was concluded that defects arise in the unstable wave field as a consequence of the large spanwise extent of the flow and the relatively broadband character of the natural excitation. Slightly different frequencies (different wavelengths) were presumed to arise and grow simultaneously over different portions of the span. These developing 'vortex patterns' can never match perfectly, and dislocations as in figure 1 are the necessary result.

1.2. *Scope of the present study*

It is impossible to follow the evolution of a single defect as it travels downstream – at least not with hot wires in a wind tunnel. One alternative is to produce a series of defects by means of acoustic forcing. Since the individual members in a series of acoustically forced defects are observed to be nearly identical, the evolution of a single defect can be reconstructed with reasonable approximation by the superposition of many defect passages. Three distinct types of forcing are employed. The first consists of forcing at two frequencies f_1 and $f_2 = f_1 + 10\%$, where f_1 is the natural, most unstable frequency. We imagine this forcing to correspond most closely to the unforced, natural evolution. Results for this case are also discussed in Yang *et al.* (1993). Here, two other cases involving subharmonics are also considered – one in which the subharmonic $\frac{1}{2}f_2$ is applied, and one with application of both $\frac{1}{2}f_1$ and $\frac{1}{2}f_2$. Typical results for the three forcings are shown in figure 2 for two stations – the first at 1.2 wavelengths and the second at 3.0 wavelengths downstream. The longitudinal fluctuation field is shown as a function of time (vertical coordinate) and span (horizontal coordinate). The right and left columns correspond respectively to the two measurement positions: $y = +\delta$ above the flow centreplane on the low-speed edge, and $y = -\delta$ below the flow centre-plane on the high-speed edge. (δ is the mixing-layer thickness.) Each field is constructed as a superposition of twenty individual defect passages (sixty span measurement positions using a three-hot-wire array moved laterally). Solid lines correspond to positive fluctuation; dashed lines correspond to negative fluctuation. The small-scale wiggles that are evident along the wavefront are near the Nyquist scale and are a measure of the variations to be expected among the individual members of the superposition.

The resulting flow developments depicted in figure 2(*a*) are surprising. In the absence of explicit subharmonic forcing, the region surrounding the defect is the most active portion of the mixing layer, and is the site of a *local* scale change to larger scales. The scale change is just beginning at three wavelengths downstream. The same features are present in the patterns recorded above and below the centreplane. The vicinity of the defect is the region of lowest amplitude for the fundamental pattern. Thus, subharmonic scales first appear where the fundamental pattern is weakest and not where it is strongest. Nonlinearity is not always associated with the largest-amplitude disturbances.

Figure 2(*b*, *c*) suggest that the localized process can be significantly altered by the imposition of additional subharmonic forcing. The subharmonic is most clearly present over a region of larger extent when $\frac{1}{2}f_1$ and $\frac{1}{2}f_2$ are both applied, as in figure 2(*c*). This is to be expected. The subharmonic content is also more evident on the low-speed edge of the flow (right panels in figure 2*b*, *c*). There is no fundamental difference in viewing the process from either of the two edges, but the subharmonic development on the high-speed side lags development on the low-speed side. At 3.5 wavelengths downstream the pattern on the high-speed side closely resembles the right panel of figure 2(*c*).

The quantitative characterization of such a localized scale change is not simple. In fact, it motivated our interest in the wavelet transform, which is precisely suited to perform a localized Fourier analysis. A new, non-direction-specific wavelet – termed the Arc wavelet – was developed for data analysis. The Arc wavelet transform will resonate with localized wave energy irrespective of the physical orientation of the wave field. This and many other useful properties are described in Dallard & Spedding (1992). In a related paper, Spedding, Dallard & Browand (1991) briefly

(a)

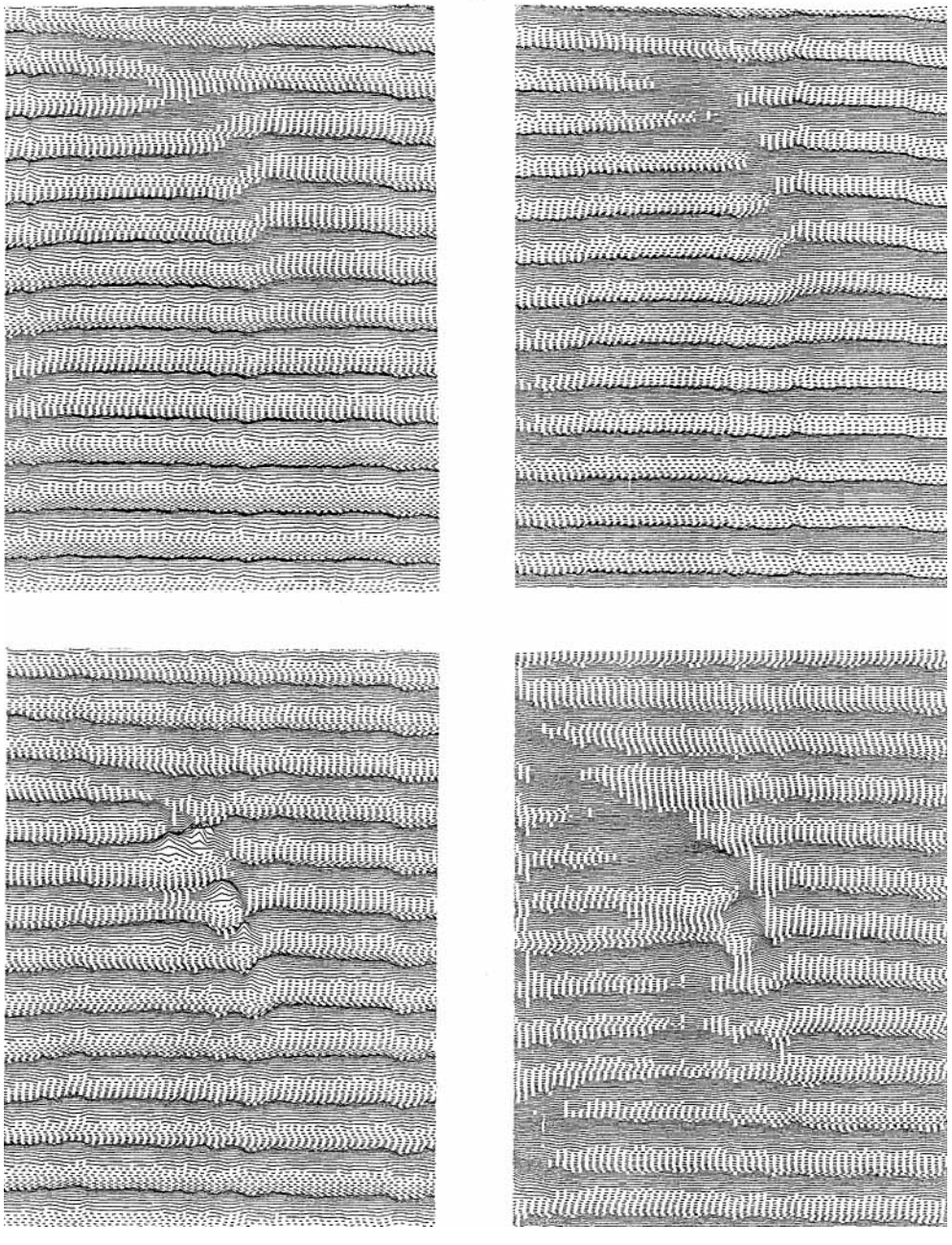

FIGURE 2(a). For caption see facing page.

compare the performance of several common wavelet transforms applied to the turbulent shear flow and to large, homogeneous, two-dimensional turbulent fields.

Because the present analysis depends so heavily upon an understanding of this relatively new technique, the main features of the Arc wavelet transform will be described in §2. Section 3 discusses the experimental set-up, and details of the forcing technique. Sections 4–6 contain the principal results and a discussion.

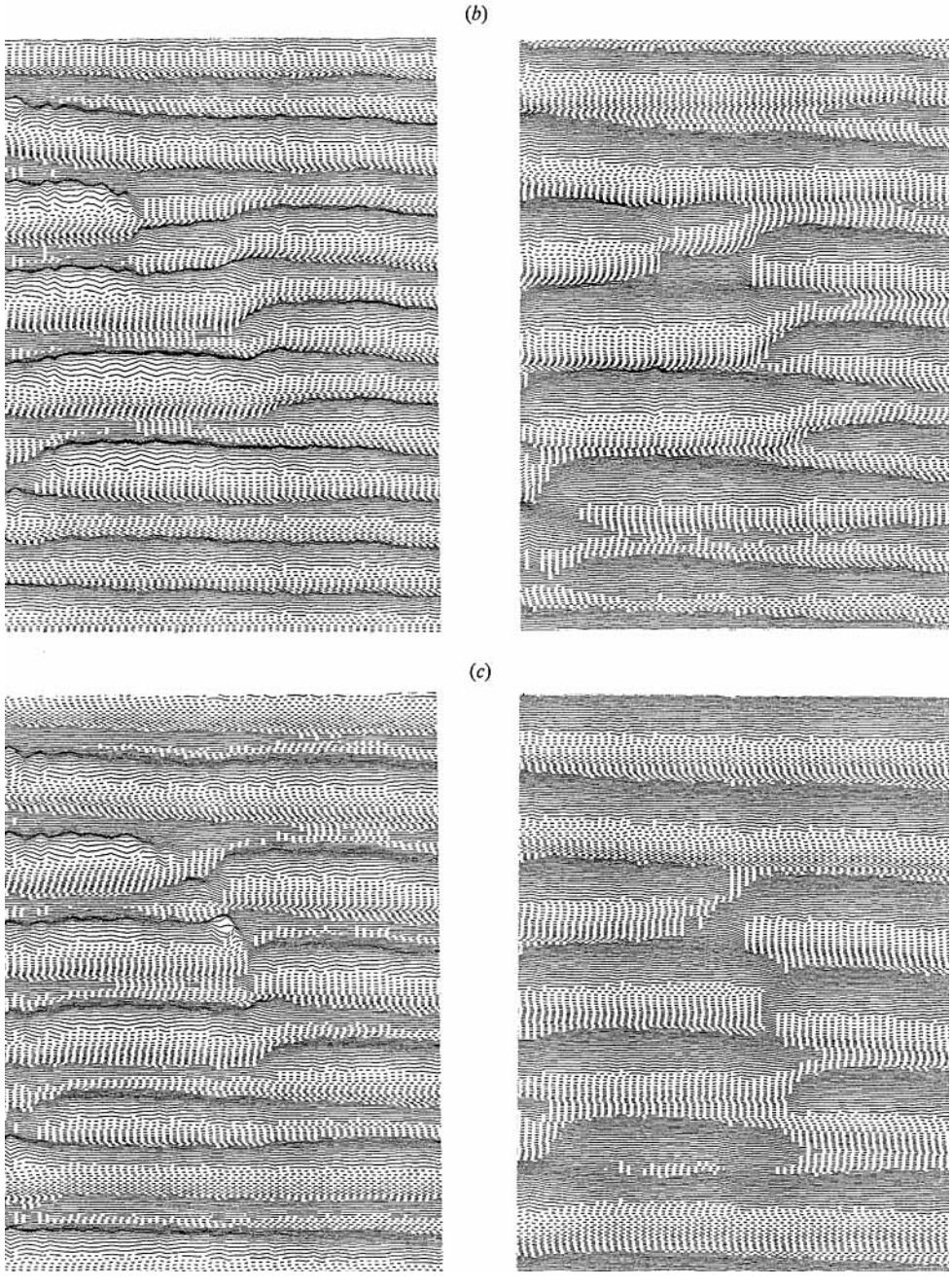

FIGURE 2. Two-level contour plot of velocity fluctuation, u'. Right column: $y = \delta$ above the centreplane (low-speed edge); Left column: $y = -\delta$ below the centreplane (high-speed edge); (*a*) case I (forcing at f_1 and $f_1 + 10\% = f_2$), upper row $x = 1.2\lambda$, lower row $x = 3.0\lambda$; (*b*) case II (forcing at f_1, f_2 and $\frac{1}{2}f_2$), $x = 3.0\lambda$; (*c*) case III (forcing at f_1, f_2, $\frac{1}{2}f_1$ and $\frac{1}{2}f_2$), $x = 3.0\lambda$. Solid lines are positve fluctuation, dotted lines are negative fluctuation.

2. The wavelet transform

2.1. *Elementary properties of wavelets*

The wavelet transform of f in $(a, \boldsymbol{b})$ is the projection of the function f on the wavelet $g_{a,\boldsymbol{b}}$ generated from a mother wavelet after translation $\boldsymbol{b}$ and dilation a. For data analysis, the mother wavelets frequently used include: the second derivative of a Gaussian (the Mexican hat, a real function); an oscillation contained within a Gaussian envelope (the Morlet wavelet, a complex function). In two dimensions, the general definition is

$$f_{\mathrm{W}}(a, \boldsymbol{b}) = \iint f(\boldsymbol{r})\, g^*_{a,\boldsymbol{b}}(\boldsymbol{r})\, \mathrm{d}\boldsymbol{r} = \frac{1}{a^2} \iint f(\boldsymbol{r})\, g^*\left(\frac{\boldsymbol{r}-\boldsymbol{b}}{a}\right) \mathrm{d}\boldsymbol{r}. \tag{1}$$

The wavelet g satisfies

$$\iint |g(\boldsymbol{r})|^2\, \mathrm{d}\boldsymbol{r} < +\infty. \tag{2}$$

The scaling factor $1/a^2$ is consistent with the requirement that

$$\iint |g_{a,\boldsymbol{b}}|(\boldsymbol{r})\, \mathrm{d}\boldsymbol{r} = \iint |g|\,(\boldsymbol{r})\, \mathrm{d}\boldsymbol{r}. \tag{3}$$

There are other possible scalings (e.g. Mallat 1989; Farge *et al.* 1990; Farge 1992). We can also give an alternative interpretation of (1) by taking the Fourier transform in the integral (Theorem of Parseval):

$$f_{\mathrm{W}}(a, \boldsymbol{b}) = \iint \hat{f}(\boldsymbol{k})\, \hat{g}^*(a\boldsymbol{k})\, \mathrm{e}^{\mathrm{i}\boldsymbol{k}\cdot\boldsymbol{b}}\, \mathrm{d}\boldsymbol{k}, \tag{4}$$

where $\hat{f}$ is the Fourier transform of f. For a given wavelet, $\hat{g}(a\boldsymbol{k})$ is known, and (4) provides a useful interpretation as well as a straightforward means for computing wavelet transforms.

The wavelet transform must also possess an inverse. This requires that the constant C_g exist:

$$C_g = \iint \frac{\hat{g}(\boldsymbol{k})\, \hat{g}(\boldsymbol{k})^*}{|\boldsymbol{k}|^2}\, \mathrm{d}\boldsymbol{k} < +\infty. \tag{5}$$

It is equivalent to the condition that the average of g vanish or $\hat{g}(0) = 0$.

A useful property derivable when (5) is met, is the isometry relationship:

$$\iint f_1(\boldsymbol{r}) f_2(\boldsymbol{r})\, \mathrm{d}\boldsymbol{r} = \frac{1}{C_g} \int_{\alpha=0}^{2\pi} \int_{a=0}^{+\infty} \iint f^{\alpha}_{1\mathrm{W}}(a, \boldsymbol{b}) f^{\alpha}_{2\mathrm{W}}(a, \boldsymbol{b}) \frac{\mathrm{d}a}{a}\, \mathrm{d}\boldsymbol{b}\, \mathrm{d}\alpha, \tag{6}$$

where f^{α} is the wavelet transform of f with g_{α}, after a rotation (angle α) of g in the physical plane. A non-direction-specific wavelet ($\hat{g}(\boldsymbol{k}) = \hat{g}(k)$) is better adapted for the interpretation of experimental results (e.g. Dallard & Spedding 1992). In such a case, there is no rotation needed, and

$$\iint f_1(\boldsymbol{r}) f_2(\boldsymbol{r})\, \mathrm{d}\boldsymbol{r} = \frac{\mu}{C_g} \iint f_{1\mathrm{W}}(a, \boldsymbol{b}) f_{2\mathrm{W}}(a, \boldsymbol{b}) \frac{\mathrm{d}a}{a}\, \mathrm{d}\boldsymbol{b}. \tag{7}$$

with

$$C_g = \int_{k=0}^{+\infty} \frac{|\hat{g}(k)|^2}{k}\, \mathrm{d}k < +\infty \tag{8}$$

and $\mu = 2$ in the case of a Hardy wavelet (as with Arc, see §2.2), or $\mu = 1$ in the general case of a cylindrical wavelet (as with Halo, §2.2).

Setting $f_1 = f_2 = f$, gives an expression for the total energy of the function f:

$$\|f\|^2 = \int |f|^2 \,\mathrm{d}\boldsymbol{r} = \frac{\mu}{C_g} \int_{a=0}^{+\infty} \iint |f_{\mathrm{W}}(a, \boldsymbol{b})|^2 \frac{\mathrm{d}a}{a} \mathrm{d}\boldsymbol{b}. \tag{9}$$

The quantity $(\mu/C_g)\,|f_{\mathrm{W}}(a, \boldsymbol{b})|^2$ can be regarded as a spatial energy density (energy per unit area) at the scale a (per unit $\mathrm{d}(\ln a)$). We will eventually compare energy densities for different ranges of scale a.

2.2. *The Hardy space wavelets*: *Morlet2D and Arc*

Returning for a minute to one dimension, the concept of envelope amplitude and phase can be extended to a function $f(t)$ containing more than a single frequency component by constructing a complex function having the original $f(t)$ as the real part, and having imaginary part equal to the Hilbert transform of $f(t)$:

$$F(t) = f(t) - \mathrm{i}H_i(f(t)). \tag{10}$$

Thus the modulus, $[f^2 + H_i(f)^2]^{\frac{1}{2}}$, is the instantaneous envelope amplitude and the instantaneous phase is $\phi = \tan^{-1}(-H_i(f)/f)$. It is easily shown that

$$\omega \leqslant 0 \Rightarrow \hat{F}(\omega) = 0. \tag{11}$$

Functions satisfying (11) are termed Hardy functions, or are said to occupy Hardy space: $F \in \mathscr{H}$. For wavelets such that $g \in \mathscr{H}$, the wavelet transform $f_{\mathrm{W}}(a, b)$ (the scale a being fixed) exists in $\mathscr{H}$ also.

The separation of envelope amplitude and phase is a useful analysis tool for one-dimensional signals. (For example, it allows the simple separation of amplitude modulation and phase or frequency modulation.) It is even more useful in several dimensions where phase information alone may reveal patterns at certain scales – even in the presence of significant noise. However, the concept of a Hardy function is not uniquely extendable to two dimensions; thus there is considerable latitude in deciding how this extension might be accomplished (Dallard & Spedding 1992).

One extension (for the Morlet wavelet of Grossman & Morlet 1984) is to assign a spatial orientation to the wave packet, creating *Morlet2D*:

$$g_\alpha(\boldsymbol{r}) = \exp(\mathrm{i}\boldsymbol{k}_0 \boldsymbol{r}) \exp(-|\boldsymbol{r}|^2/2\sigma^2) \tag{12}$$

and

$$\hat{g}_\alpha(a\boldsymbol{k}) = \exp(-\tfrac{1}{2}[a^2\sigma^2(\boldsymbol{k} - \boldsymbol{k}_0/a)^2]), \tag{13}$$

where the product $\sigma|\boldsymbol{k}_0| = \sigma k_0$ determines the number of waves in the packet (often chosen to be $\sigma k_0 \sim 5$, so that the admissibility condition $\hat{g}(0) = 0$ is almost satisfied) and α is the orientation of the vector $\boldsymbol{k}_0$. The Morlet2D is shown in wavenumber space in figure 3(*a*) for $\alpha = 0$). To cover the wavenumber plane using Morlet2D, many values of α must be chosen. When there is a clearly perceived directionality to the space pattern, $f(\boldsymbol{r})$, the appropriate α is known and a single value may be sufficient. Often, however, the pattern is obscured or may have different orientations at different scales (as in our case). A wavelet possessing additional symmetry in the physical plane, so as to be sensitive to $f(\boldsymbol{r})$ containing waves of many orientations, would be most useful. In wavenumber space, the proposed wavelet should thus possess a Fourier transform providing maximum coverage of the plane as the parameter a varies. A class of symmetric wavelets has the Fourier transform

$$\hat{g}(a\boldsymbol{k}) = \hat{g}(ak) = \exp(-\tfrac{1}{2}[a^2\sigma^2(k - k_0/a)^2]), \tag{14}$$

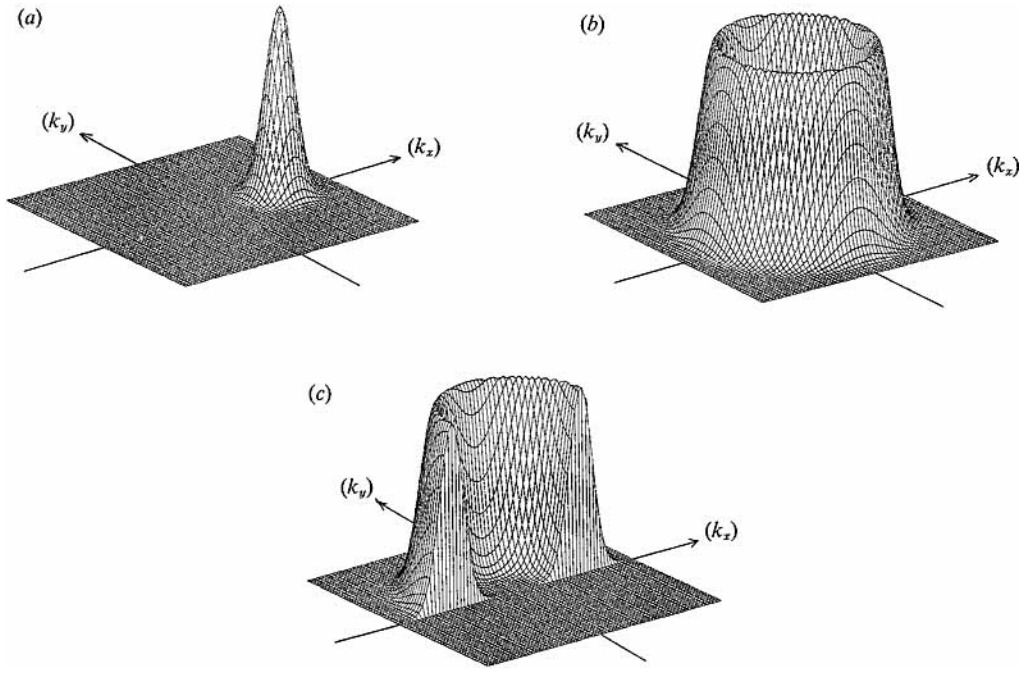

FIGURE 3. (a) The Fourier transform in $[k_x, k_y]$ of: (a) Morlet2D; (b) Halo; (c) Arc.

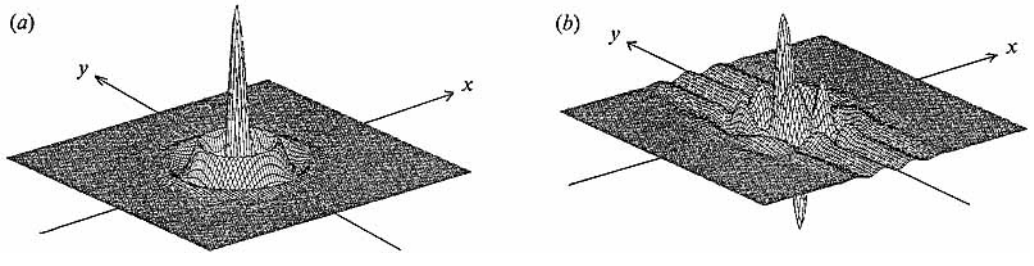

FIGURE 4. Representation of the Arc wavelet in space coordinates $[x, y]$: (a) real part; (b) imaginary part.

as shown in figure 3(b). It will be referred to as the *Halo*. The Halo is displaced from the origin by radius k_0/a and has breadth $1/(\sigma a)$ along a radial direction in the $\boldsymbol{k}$-plane. As the wavelet scale varies, the entire $\boldsymbol{k}$-plane is covered. However, the resulting wavelet transform is purely real, without the useful property of phase and envelope amplitude separation. To create phase and amplitude information, one must ensure $g_{a,\boldsymbol{b}}(\boldsymbol{r})$ exists in $\mathscr{H}$, which means restricting the contributions of $g(\boldsymbol{k})$ to a half-plane. Such a possibility is shown in figure 3(c). This is an example of the Arc wavelet. The Arc depicted here has the Fourier transform

$$\hat{g}(\boldsymbol{k}) = \hat{g}(k) = \exp\left(-\tfrac{1}{2}[a^2\sigma^2(k-k_0/a)^2]\right) \quad \text{if} \quad k_y > 0, \tag{15}$$

$$\hat{g}(\boldsymbol{k}) = 0 \qquad\qquad\qquad\qquad\quad \text{if} \quad k_y < 0. \tag{16}$$

The Arc wavelet is illustrated in figure 4(a, b) in space coordinates. The real part of the wavelet is axisymmetric and diminishes rapidly away from the origin. The

imaginary part is not symmetric and is not as well localized in space. Although the bulk of the wavelet consists of a collection of peaks near the origin, a 'tail' is seen to extend preferentially along the y-axis. The orientation of the tail is related to the orientation of the Arc in wavenumber space, and the magnitude is related to the sharpness of the cutoff near $k_y = 0$. Some degree of asymmetry is the price one pays for the convenience of defining a complex wavelet. These peculiarities should be kept in mind, but they do not diminish the utility of the transform. Wavelet energy is still highly localized in space – 92.5% of the Arc wavelet energy is contained within a circular distance of radius $\sqrt{2}a$ from the origin, while the Morlet wavelet contains 86.5% for the same radius. When possible, however, the partition should be made in wavenumber space along a direction for which the field under analysis, $\hat{f}(\boldsymbol{k})$, contains small contributions (Dallard & Spedding 1992).

3. Experimental arrangement; analysis procedures

3.1. *The space–time data set*

The mixing layer is produced in a wind tunnel having geometry and dimensions sketched in figure 5(*a*). The turbulent region to be studied exists immediately downstream from the splitter plate dividing the two streams of speeds $U_1 = 16.5$ m/s and $U_2 = 5.8$ m/s, respectively. The non-dimensional speed ratio $R = (U_1 - U_2)/(U_1 + U_2) = 0.48$. The initial flow structure is forced acoustically utilizing a pulse train of finite duration applied to sixteen loudspeakers arranged along the span in the wind tunnel ceiling. Direct measurement of the pressure field at the splitter-plate trailing edge verifies that the acoustic velocities here are of the order of a few millimetres per second. Thus the level of forcing, expressed as a fraction of the maximum flow velocity, is $1\text{–}2 \times 10^{-4}$. This small forcing is sufficient to impose local order upon the growing instability.

The longitudinal velocity fluctuation is measured as a function of span by translating a rake of three hot wires positioned along the span (see figure 5*a*). The imposed acoustic pulse train provides the origin in time; repetitions of the train produce (nearly) identical flow responses. After each repetition, the hot-wire rake is moved laterally until a matrix of sixty span locations has been accumulated (a superposition of twenty separate repetitions). The total span covered is $40.2\lambda_1$, where λ_1 is the wavelength of the forced wave: $\lambda_1 = 1.79$ cm. (It is within a few tenths of a per cent of the most unstable wave in the developing flow, observed to arise naturally in the absence of any forcing.) The spanwise separation between measurement points is $\delta z = 1.2$ cm. At each span position, a time series is recorded for the interval $\Delta T = 1024\delta t$ ($\delta t = 80$ ms). A space–time series z–t is thus accumulated at each of twelve downstream locations from $Rx/\lambda_1 = 0.3$ to 3.6 in increments of 0.3. For each span position and each downstream location, the means have been subtracted and the signal levels normalized by the signal in a time interval $200\delta t$ beginning at approximately $200\delta t$. This region is unaffected by the presence of the defect, and is later referred to as the *external region*. When moving from one downstream position to the next, the hot-wire array is fixed along the ray $y/x = 0.15$, corresponding to a location about one maximum slope thickness about the centreplane of the layer (on the low-speed side). Being near the outer edge of the mixing layer ensures sensitivity to the largest scales in the flow, and decreases sensitivity to the smaller scales. This is an important point. The data do not contain smaller-scale fluctuations which are certainly present in the interior of the mixing layer. The phenomena observed here are not sensitive to the precise hot-wire

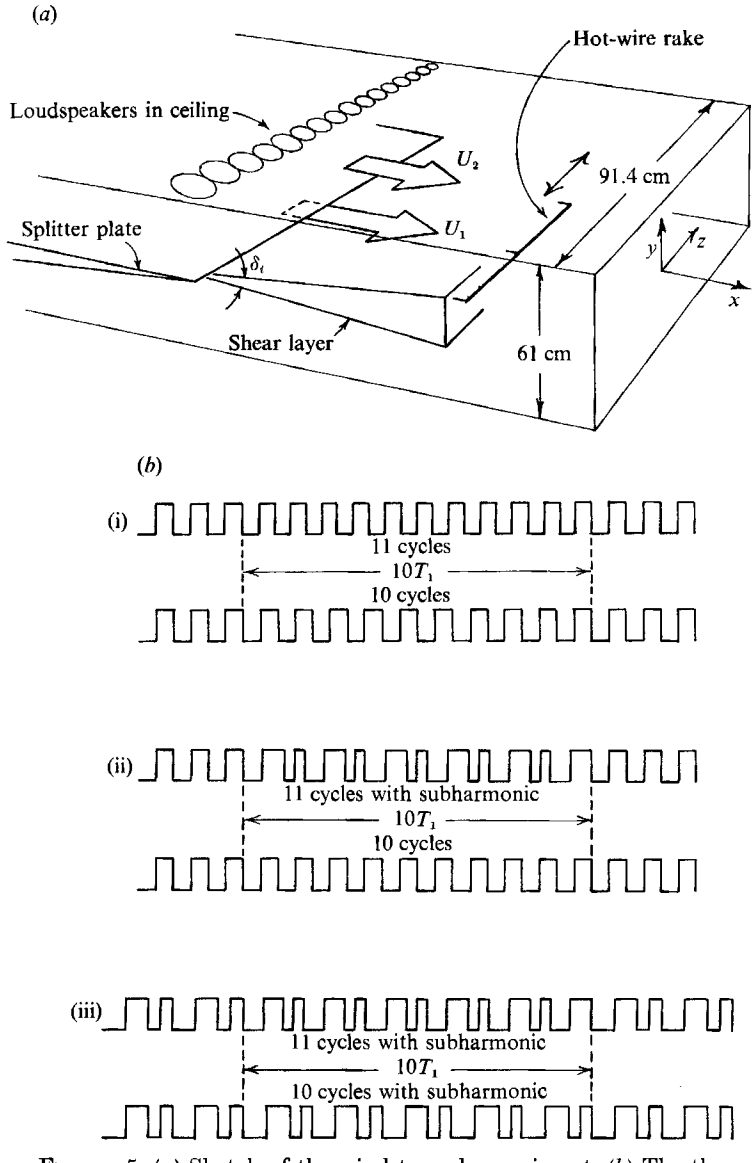

FIGURE 5. (a) Sketch of the wind tunnel experiment. (b) The three sets of pulse trains utilized in the acoustic forcing.

location. Figure 2 contains data recorded on the high-speed side of the mixing layer at approximately the same distance from the central plane ($y/x = \pm 0.15$). Aside from the expected phase shift of 180°, the images recorded on either side are quite similar.

3.2. *Details of the acoustic forcing*

The forcing is produced by two separate trains of fixed-amplitude pulses. The two trains have the same total time length. The first twenty pulses and the last twenty pulses are identical, but the middle ten pulses are different. Three distinctly different combinations are utilized, as sketched in figure 5(b). Case I is the simplest. For train

1, all fifty pulses of period T_1 are identical. The duty cycle is one-half, and the frequency, f_1, is 623 Hz. The most amplified frequency in the naturally developing laminar flow is 625 Hz. In the interior interval, $10T_1$, train 2 contains eleven pulses (corresponding to a frequency $f_2 = 685$ Hz), 10% higher than f_1. Train 1 is applied to eight speakers on the right half of the tunnel, and train 2 is applied to the eight left-half speakers. The result of the forcing is the defect in structure shown in figure 2(*a*) at $Rx/\lambda_1 = 0.6$.

For case II, train 1 is identical to case I. But to train 2, the subharmonic of f_2 is added in the interior interval $10T_1$. This is accomplished by modulating the pulse width. Each pulse is alternately lengthened or shortened by 27% of the original length, and might be expected to produce a subharmonic component shifted forward in phase by perhaps $0.10T_1$ (cf. Monkewitz 1988). For case III, all pulses of width T_1 in trains 1 and 2 are pulse-width modulated to include the subharmonic of f_1 (in addition to the subharmonic of f_2).

3.3. *Utilizing the Arc wavelet transform*

For each of three forcings and for each of 12 downstream positions, we have a two-dimensional data array (time × span) having dimension $(51T_1 \times 40.2\lambda_1)$, where T_1 is the period corresponding to f_1 ($T_1 = 0.001605$ s $= 20.06\delta t$) represented by (1024×60) points. We isolate a smaller array containing 512 time points centred on the original defect as it advects downstream at speed $\bar{U} = \frac{1}{2}(U_1 + U_2)$. Only 55 span points are kept to avoid unwanted influence from the sidewalls. Since it is convenient to work with an array of larger z dimension, the span array is expanded to 256 points by performing a spline interpolation along z for each time step. (Fourier transforms of the two data sets show no significant differences. At low wavenumbers, where there is significant energy, the spectral amplitudes are different by $O(5 \times 10^{-3})$ on a scale of unity. At higher wavenumbers, the differences are $O(10^{-3}$–$10^{-4})$, of the order of the noise components in the raw data.) Thus the wavelet transform is applied to $(N = 512 \times M = 256)$ points corresponding in (time × span) to $(25.5T_1 \times 37\lambda_1)$. Notice that the array is distorted. An equivalent convection length is $\delta X = \bar{U}\delta t$. A capital X is used here as a reminder that X is an equivalent lengthscale and not the physical dimension x. Then $T_1 = 20.06\delta t$ correspond to an equivalent space discretization $\lambda_1 = 20.06\delta X$. Since $\lambda_1 = 6.92\delta z$ (after interpolation), δz and δX are in the ratio $\delta z = s\delta X$, $s = 2.90$. This scale ratio must be incorporated in the wavelet transform to ensure that two-dimensional space is treated consistently.

It is necessary to be specific about the choice of values for the scale parameter a. The procedure is illustrated with the Arc wavelet, although the argument is perfectly general. The principal wavenumber vector for the fundamental pattern lies close to the k_X axis. It is convenient to take the partition well away from this direction (Dallard & Spedding 1992): the choice will be to put the partition along the k_z axis. The Arc wavelet used is given by

$$\hat{g}(a\boldsymbol{k}) = \exp\left(-\tfrac{1}{2}[a^2\sigma^2(k - k_0/a)^2]\right) \quad \text{if} \quad k_X > 0, \tag{17}$$

$$\hat{g}(a\boldsymbol{k}) = 0 \quad \text{if} \quad k_X < 0. \tag{18}$$

It is also convenient to express all physical scales $\boldsymbol{r}$, $\boldsymbol{k}$, k_0 in terms of the fundamental space (time) unit δX (δt). This choice effectively fixes the value of σ, $\sigma = \delta X$ (δt). The choice $\sigma k_0 = 5.5$ is also made, to give $k_0 = 5.5/\delta X$. Arc is then completely defined.

The data set possesses a pattern at the fundamental wavelength λ_1, corresponding to wavenumber $k_1 = 2\pi/\lambda_1$. This value corrsponds to a scale a_1 given by

$$a_1 = \frac{k_0}{k_1} = \frac{k_0 \lambda_1}{2\pi} \sim (0.875)\frac{\lambda_1}{\delta X}. \tag{19}$$

Since for our data $\lambda_1 = 20.06\delta X$ (δt implied), the corresponding resonant scale is

$$a_1 = (0.875)\,20.06 = 17.56. \tag{20}$$

The smallest scale resolvable in the data is $\lambda_{\min} = 2\delta X$, a result of the Nyquist criterion. The smallest value of a, $a_{\min}$, needs be no smaller than $a_{\min} = 1$.

To choose the spacing of a values, recall that the Arc wavelet interrogates a region of wavenumber space of size $1/\sigma a$ about the value k_0/a. Discrete values of k_0/a need not be spaced closer than, say, $\delta(k_0/a) = 1/(4\sigma a)$ leading to the result

$$da/a = a/(4k_0\sigma). \tag{21}$$

The number of required values per octave, m, is simply

$$m = 4k_0\sigma \ln 2, \tag{22}$$

which is close to 16 for $k_0 = 5.5/\delta X$. A rule of thumb would be 16 scales per octave (spaced logarithmically) for as many octaves as are required to span the data.

3.4. *Cones of influence*

The wavelet transform $f_W(a, \boldsymbol{b})$ resides in the physical parallelepiped

$$\delta X < b_X < N\delta X, \tag{23}$$

$$\delta X < b_z < Ms\delta X, \tag{24}$$

$$1 < a < N. \tag{25}$$

The data set, $f(\boldsymbol{r})$, lies in the rectangular base domain

$$\delta X < r_X < N\delta X, \tag{26}$$

$$\delta X < r_z < Ms\delta X. \tag{27}$$

Some of the values $f_W(a, \boldsymbol{b})$ for $1 < a < N$ depend upon values $f(\boldsymbol{r})$ which lie outside the original base domain, and depend upon how the functional values are continued. For example, methods based upon Fourier series (such as the FFT) assume periodicity to extend $f(\boldsymbol{r})$ into the exterior region. To be free from spurious continuations, we must ask in what domain $(a, \boldsymbol{b})$ is $f_W(a, \boldsymbol{b})$ entirely dependent upon $f(\boldsymbol{r})$ within the original domain $[r_X, r_z]$. The value $f(\boldsymbol{r}_0)$ will influence $f_W(a, \boldsymbol{b})$ in a domain $[b_X, b_z]$ bounded by $|\boldsymbol{r}_0 - \boldsymbol{b}|/a = O(1)$ which is a cone of nominal radius a extending upward from $\boldsymbol{r}_0$. So the boundaries of the original base domain $[1, N] \times [1, M]$ will influence $f_W(a, \boldsymbol{b})$ for $\boldsymbol{b}$ outside the domain $[a, N-a] \times [a/s, M-a/s]$. For this reason, the value of $a_{\max}$ must be chosen to leave a sufficiently large domain $[b_X, b_z]$. We have chosen $a_{\max} = \frac{1}{5}N \approx 100$. All values $f_W(a, \boldsymbol{b})$ lying within $[a_{\max}, N-a_{\max}] \times [a_{\max}/s, M-a_{\max}/s]$ are determined by the original data set, for all values of a in $[1, a_{\max}]$. The data are sufficient to examine the scale parmeter a over roughly seven octaves, and according to (22), a total of approximately 112 values are

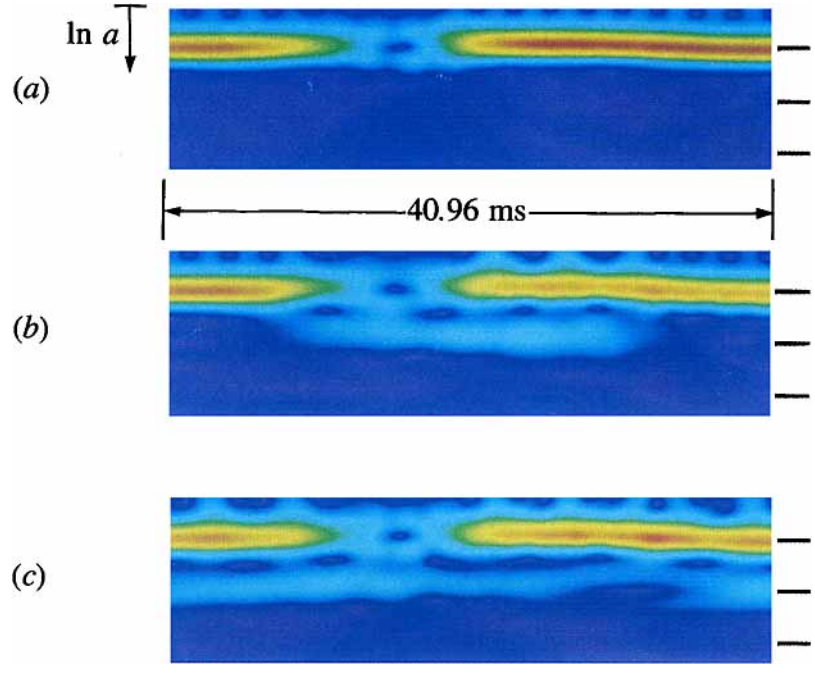

FIGURE 6. Sections of the modulus of the transform through the spanwise position of the defect at $Rx/\lambda_1 = 0.6$: (*a*) case I; (*b*) case II; (*c*) case III. The three bars refer to $a_1 = 17.56$, $2a_1 = 35.12$, $4a_1 = 70.24$. The smallest scales are at the top of each colour graph.

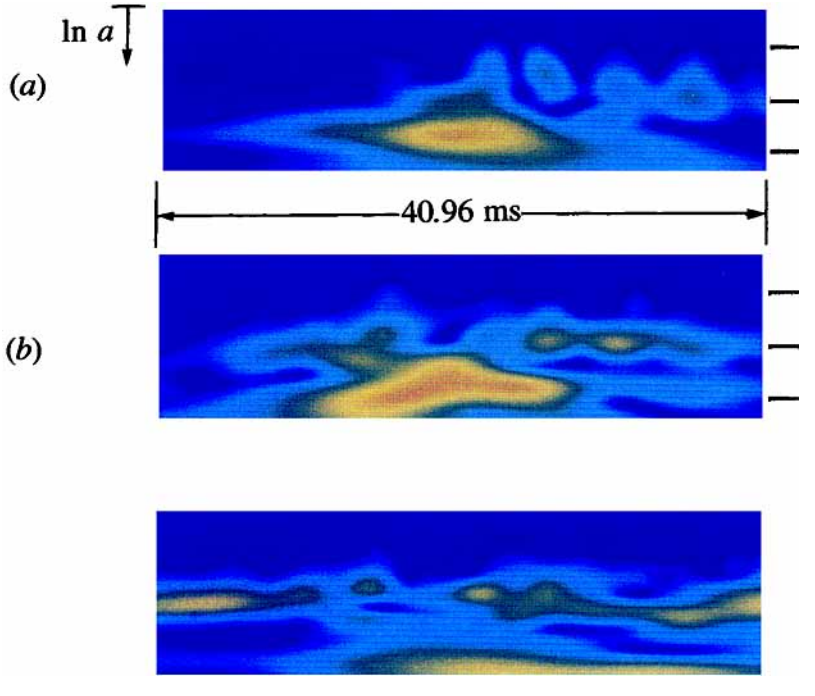

FIGURE 7. Modulus for $Rx/\lambda_1 = 1.2$ (see caption to figure 6).

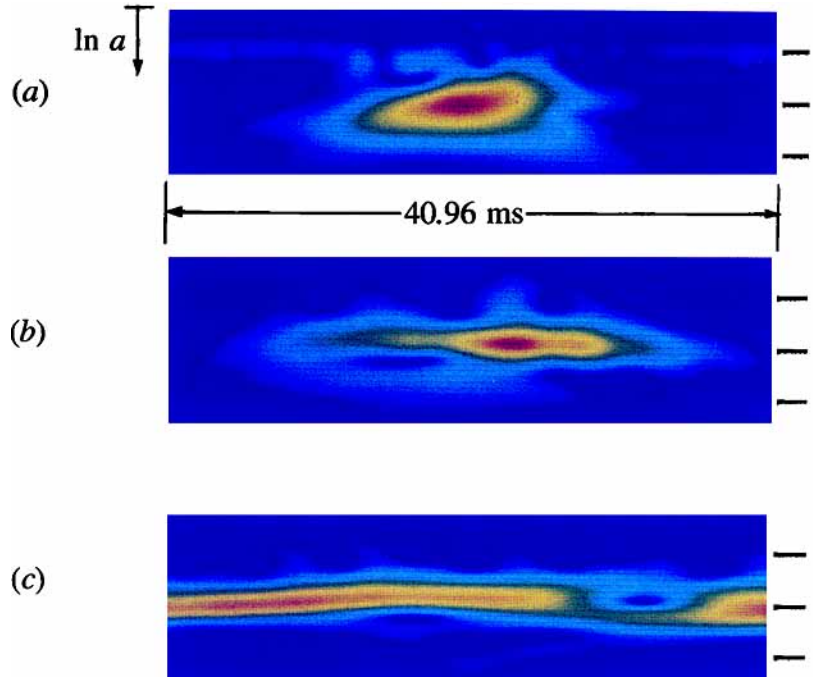

FIGURE 8. Modulus for $Rx/\lambda_1 = 1.8$ (see caption to figure 6).

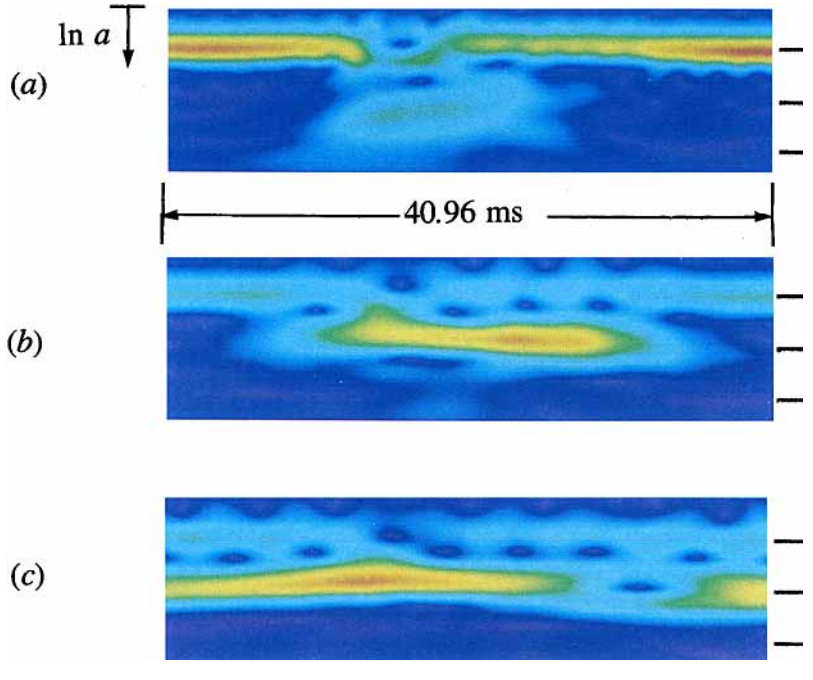

FIGURE 9. Modulus for $Rx/\lambda_1 = 3.0$ (see caption to figure 6).

needed – spaced logarithmically from 1 to 100. The scale a_1 associated with the fundamental pattern is $a_1 = 17.56$. The subharmonic will appear at $2a_1 = 35.12$, and the subharmonic of the subharmonic at $4a_1 = 70.24$. In the following calculations, we have distributed 90 values of scale a between $a = 10$ and 95.

4. An overview of downstream development utilizing the wavelet transform modulus

4.1. *Visualizations*

The colour plates 1 and 2 – figures 6–9, representing the three distinct forcings – are sections of the modulus of the transform $(N\delta X \times m\delta a/a, 65s\delta X)$ for different downstream stations. The cuts $M = 65$, are made through the spanwise position of the original defect. (Recall that δX is the time interval $\delta X = \bar{U}\delta t$.) Four identical downstream stations are displayed for each forcing condition. Consider case I containing no explicit subharmonic forcing. Initially, the scale is strongly localized at $a = 17.56$, corresponding to the forcing at f_1. (Scale $a = 16.0$ corresponding to f_2 does appear, but only in a localized region of span not displayed here.) The defect is the region of diminished amplitude in figure 6(*a*). The modulus must be exactly zero at the centre of the defect to avoid an unphysical singularity (cf. Berry 1980). The initial distributions of scale are similar for the two other forcings, figure 6(*b*, *c*), although there does exist wave energy at the subharmonic scale. The downstream development is quite different for the three cases. With no subharmonic forcing, figures 7(*a*), 8(*a*), 9(*a*) show a dramatic increase in the large scales in the vicinity of the defect. The scale cascade is centred roughly at the scale associated with the subharmonic, but it is clearly a broadband process. The subharmonic forcing at $\frac{1}{2}f_2$ (case II), which might be termed a localized subharmonic forcing, accentuates the scale transition in the defect region, figures 7(*b*), 8(*b*), 9(*b*). Here the scale change is more closely centred at the subharmonic, the physical size of the subharmonic region is larger, and the relative amplitude of the growing subharmonic is greater. Compare, for example, the subharmonic colour contours with those of the fundamental scale far from the defect. In contrast, the application of subharmonic forcing at $\frac{1}{2}f_2$ and $\frac{1}{2}f_1$ (case III), which might be termed a global application of subharmonic forcing, suppresses the role of the defect. The transition to larger scales takes place nearer the origin than for cases I and II, but the defect region remains relatively undistinguished. One interesting feature not present in the other cases is the formation of a new defect region in the subharmonic pattern. It is represented by the 'hole' in subharmonic amplitude just downstream of the original defect region in figures 7(*c*), 8(*c*). The subharmonic defect can be weakly discerned at the first downstream station, figure 6(*c*), and may have been introduced by the forcing, although it was not planned. It appears possible to introduce defects at several scales, and to have them grow to a dynamically significant strength at different downstream positions.

4.2. *Estimates of average scale*

In an effort to be more precise about the range of scales in the defect region, the following procedure is adopted. A roughly square area $(10T_1 \times 12\lambda_1)$ centred upon the original defect contains the most energetic portions of the flows. At each point, the wavelet transform modulus is scanned in the 'a' direction to find the scale which maximises $|f_W|$. These scale values are averaged over the area to give the means plotted in figure 10 as a function of downstream position.

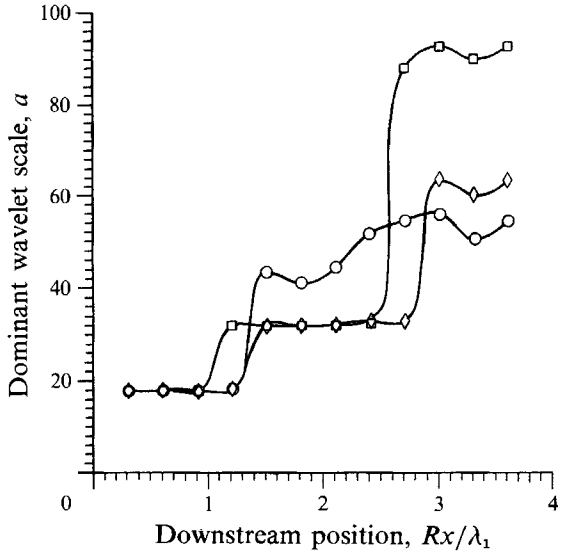

FIGURE 10. Evolution of the scales in the defect region: ○, case I; ◇, case II; □, case III.

The significant scales are plateaux connected by sharp transitions in scale. With no subharmonic forcing, the development of the subharmonic is least well organized. The first transition is to an average scale which is approximately 20% greater than the scale corresponding exactly to the subharmonic. Thereafter the scale continues to increase slowly. For cases II and III the forcing reorganizes the pairing around a particular scale a close to $2 \times a_2 \approx 32$ (as can be observed in figures 6–9). For case II forcing, a second transition to the scale corresponding roughly to $4 \times a_2 \approx 64$ takes place. Forcing globally at the subharmonic creates a rapid transition to scales which are 20–30% larger than $4a_1 = 72.24$ – reminiscent of the (unforced) transition in case I. The averaged wavelet scales associated with this last transition are only approximate, since it is clear from figure 9(*c*) that some of the scale information at this station (and beyond) lies outside the domain of the transformed results. Longer data records would be needed to examine larger values of a (cf. §3.4).

5. Distributions of energy density and excess energy density

The visualization in §4.1 can be given more precision with the aid of the definition of energy density. First consider the *external* region far from the defect, where the field is spatially uniform. Since the velocity fluctuation data are normalized by these external r.m.s. values, the total energy density in this region is exactly unity. That is

$$e_{\mathrm{XT}} \equiv \frac{2}{C_g}\int_0^\infty |f_{\mathrm{W}}(a,z,X)|^2 \frac{\mathrm{d}a}{a} = 1. \tag{28}$$

The *partition* of energy density among three non-overlapping scale intervals – centred at the fundamental (a_1), subharmonic ($2a_1$) and subsubharmonic scales ($4a_1$) – are shown in figure 11(*a–c*) for the three forcing cases. These densities are defined by

$$e_{\mathrm{XT_p}} \equiv \frac{2}{C_g}\int_{a_l-\frac{1}{3}a_l}^{a_l+\frac{1}{3}a_l} |f_{\mathrm{W}}(a,z,X)|^2 \frac{\mathrm{d}a}{a}. \tag{29}$$

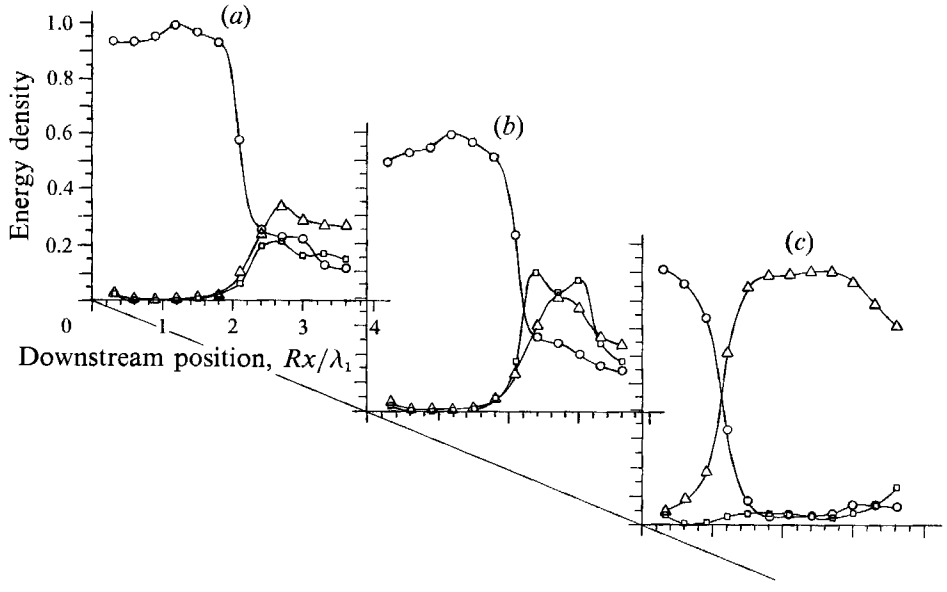

Rx/λ_1	0.3	0.6	0.9	1.2	1.5	1.8	2.1	2.4	2.7	3.0	3.3	3.6
Case I(*a*)	93	88	90	99	94	92	70	71	74	65	51	48
Case II(*b*)	85	88	91	95	93	94	90	100	102	98	63	53
Case III(*c*)	100	95	93	98	99	96	97	96	97	97	93	91

FIGURE 11. Partition of energy density outside of the defect region: (*a*) case I; (*b*) case II; (*c*) case III. ○, Energy density in fundamental band; △, subharmonic band; □, subsubharmonic band. Table insert gives the 3-band energy sum.

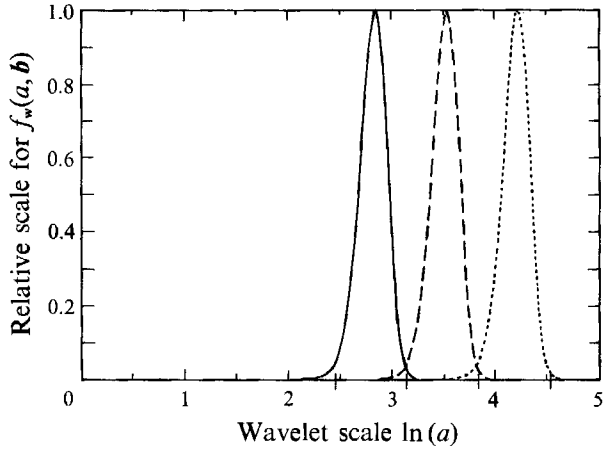

FIGURE 12. Scale distribution of the energy associated with three monochromatic waves centred at $a_1 = 17.56$, $2a_1$ and $4a_1$, corresponding to the centres of the fundamental band, subharmonic band and subsubharmonic band. The small vertical tics indicate the boundaries of each band.

(As motivation for choosing these particular upper and lower bounds, note that the wavelet transform of a *monochromatic* function $\exp^{ik_l \cdot x}$ is a Gaussian function of the scale a only, centred around $a_l = k_0/k_l$, cf. figure 12. The energy is almost totally distributed between the scales $a_l - \frac{1}{3}a_l$ and $a_l + \frac{1}{3}a_l$.) A table containing the three-band

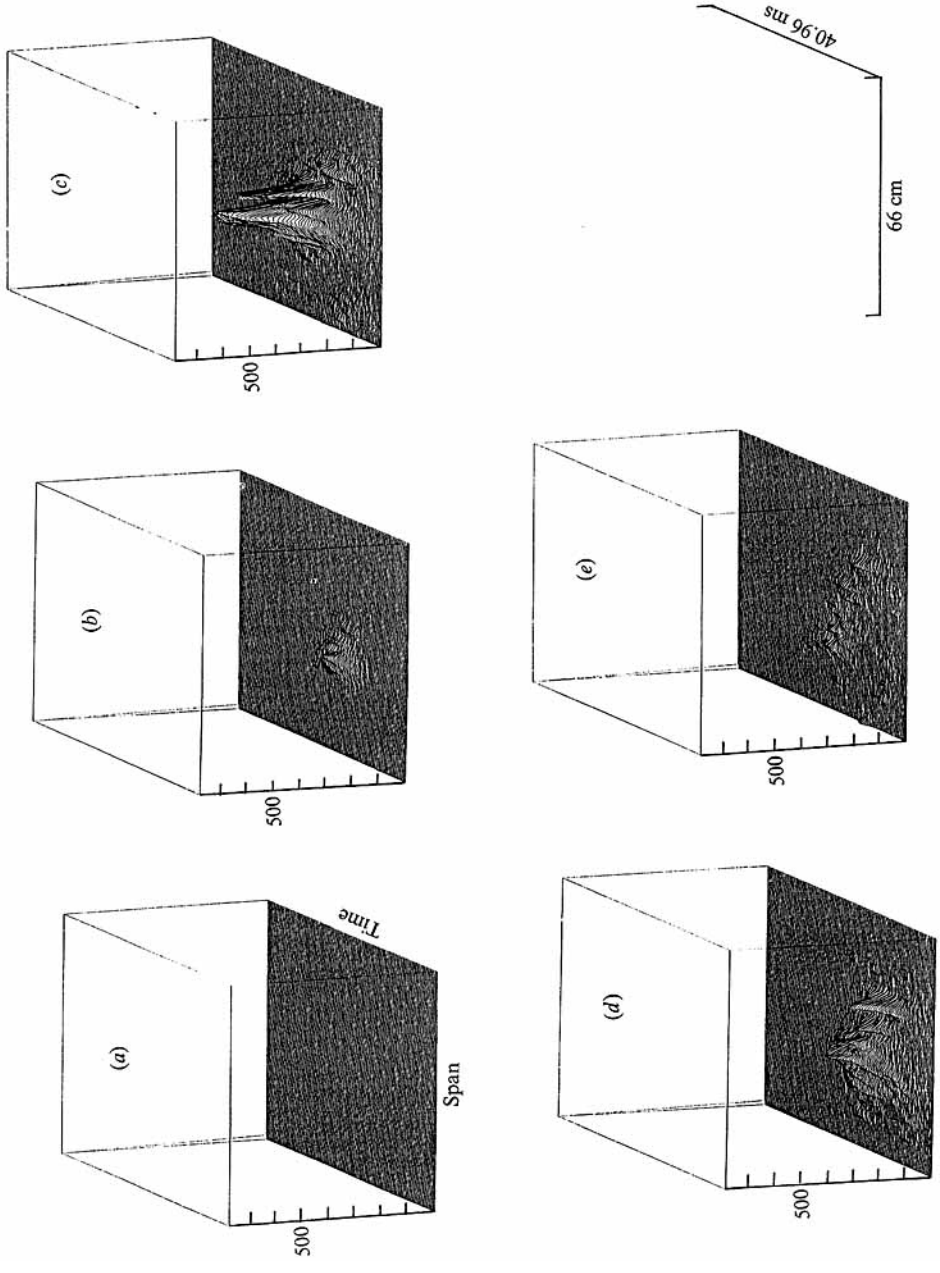

FIGURE 13. Excess energy density (case I) at: (a) $Rx/\lambda_1 = 0.6$; (b) $Rx/\lambda_1 = 1.8$; (c) $Rx/\lambda_1 = 2.4$; (d) $Rx/\lambda_1 = 3.0$; (e) $Rx/\lambda_1 = 3.6$.

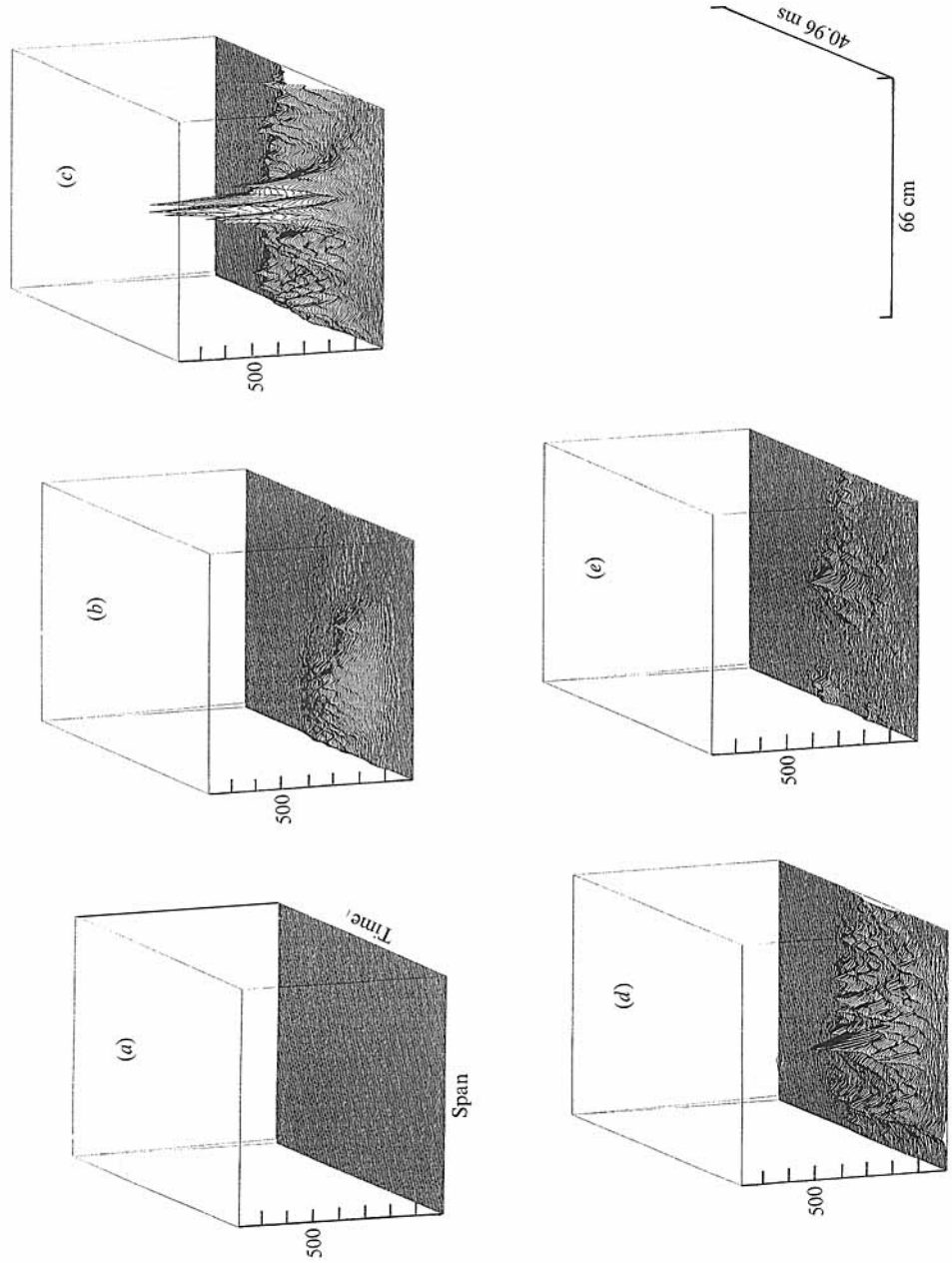

FIGURE 14. As figure 13 but for case II.

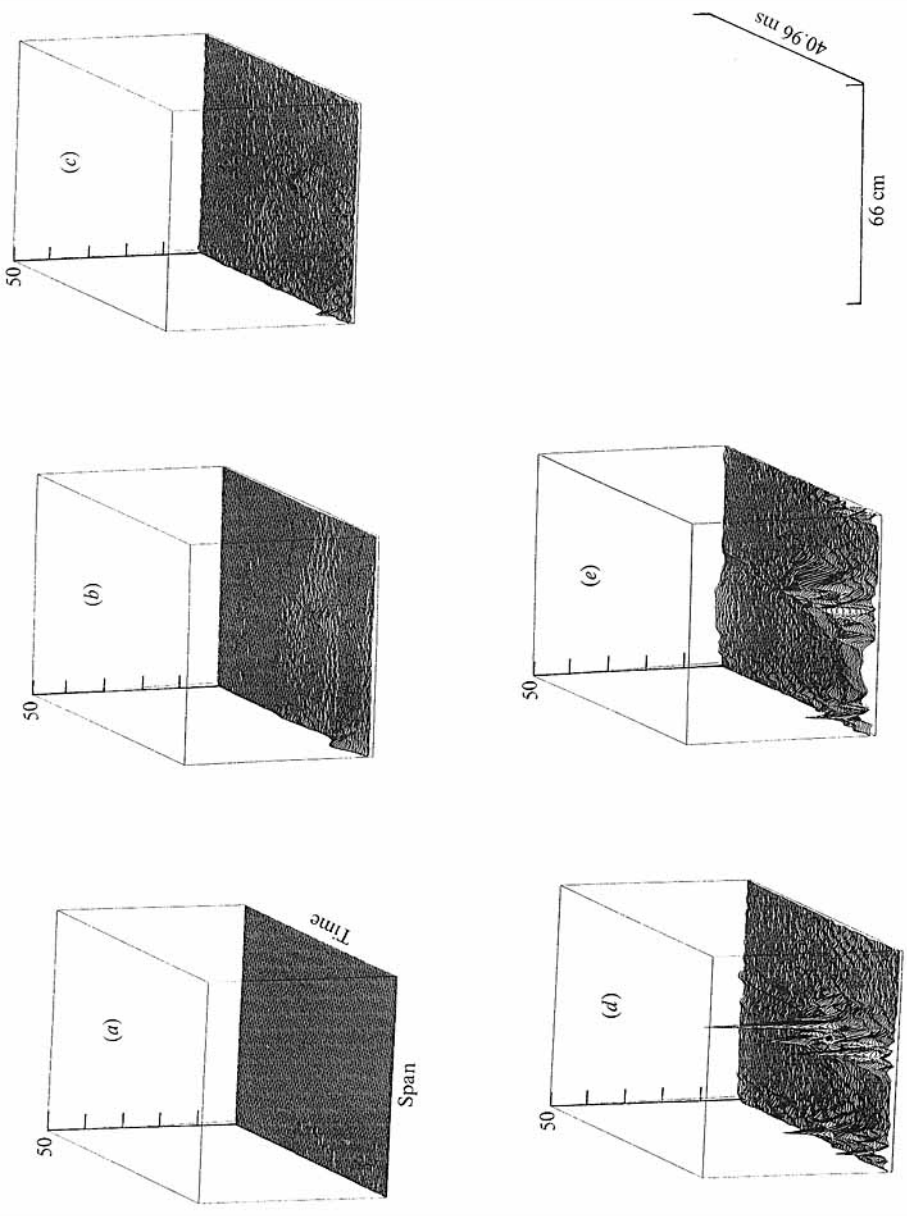

FIGURE 15*a–e*. For caption see facing page.

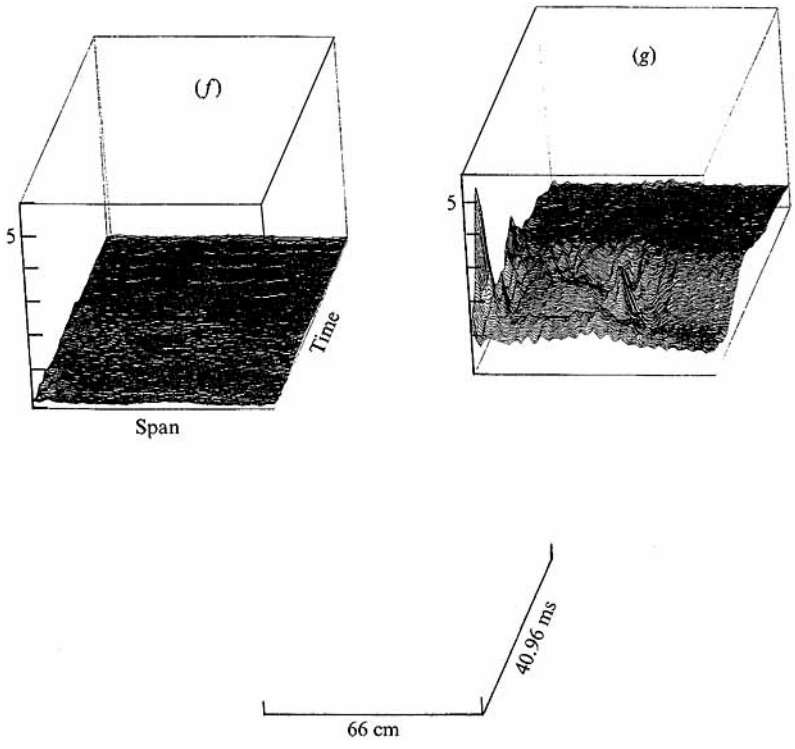

FIGURE 15. As figure 13 but for case III; note the expanded vertical scale 0–49. On a further expanded scale: (*f*) $Rx/\lambda_1 = 0.6$; (*g*) $Rx/\lambda_1 = 1.8$.

energy density sum, as a per cent fraction of the total energy, is also given for each of the downstream positions. The three bands are seen to capture the bulk of the energy in the region far from the defect, except at the most extreme downstream stations. Transfer of energy to even larger scales is probably responsible for these decreases. For case I, the energy sum fluctuates between 0.9 and 1.0 at the first few downstream stations. Since we have no explanation for these fluctuations, the variation can probably be taken as a measure of the reliability of the wavelet transform technique applied to this data set. In the region near the defect, the signal levels are higher, and the reliability should be at least as good.

Indeed, the large velocity fluctuation energies in the immediate vicinity of the defect are more interesting. For the purpose of isolating a particular area, an excess energy density is defined as the ratio of energy density in the subharmonic and subsubharmonic bands at a particular point, to the total averaged energy density in the external region. That is

$$e_{\mathrm{EXCESS}} \equiv \frac{e}{e_{\mathrm{XT}}} \equiv \frac{e}{1} \equiv \frac{2}{C_g}\int_{2a_1-\frac{2}{3}a_1}^{4a_1+\frac{4}{3}a_1} |f_{\mathrm{W}}(a,z,X)|^2 \frac{\mathrm{d}a}{a}. \tag{30}$$

This quantity is displayed as the vertical coordinate versus ($N\delta X \times Ms\delta X$) in figures 13 and 14 for cases I and II. Each figure contains the excess energy density for the five downstream stations corresponding to $Rx/\lambda_1 = 0.6$, 1.8, 2.4, 3.0, and 3.6. The vertical scale in figures 13 and 14 extends from 0 to 780. With no subharmonic forcing, there is a rapid dramatic increase in excess energy at large scales in the vicinity of the original defect region, followed by a decrease. Physically, the presence

of the defect promotes an early transition to larger scales by a *localized* pairing of vortices.† But pairing also takes place away from the defect, and because of this the excess energy density begins to decrease beyond $Rx/\lambda_1 = 2.4$. As a reference, pairing takes place in an unforced mixing layer at about $Rx/\lambda_1 \approx 2.0$, and in a mixing layer forced at a single fundamental frequency at about $Rx/\lambda_1 = 2.5$–3.0. Forcing locally at the subharmonic frequency promotes an early and more dramatic transition. At $Rx/\lambda_1 = 1.8$ (figure 14*b*), the region of significant excess energy is largely coincident with the region of applied forcing. By $Rx/\lambda_1 = 2.4$, a subregion nearest the defect clearly dominates. The peak values of excess energy here are impressive – they are as much as a factor of 500–700 greater than the external energy density. These enormous differences must be put in perspective. The measurements are made along the ray $y/x = 0.15$. In the defect region, where scales are larger, the measurement point is close to the vortex centres and the measured amplitudes are larger than in the external region where vortices are smaller (and farther removed from the measurement point). This geometrical difference accounts for at least some of the difference in wavelet amplitudes. Energy density values averaged over the entire vertical extent of the mixing layer would not show differences of 500–700 between the defection region and the external region.

With global subharmonic forcing, the situation is more complex, and is illustrated in figure 15. Note the much expanded vertical scale, 0–50. The initial growth of excess energy at the subharmonic scale can be seen in (*b*) and on a more expanded scale in (*g*). It is a slightly raised plateau preceeding the defect in time – the cross-section can be seen in figure 8(*c*). The important increases in excess energy take place farther downstream, figure 15(*d*, *e*), and are associated with subsubharmonic scales.

There is a certain consistency among the three cases. With no subharmonic forcing, the defect region is the site of an explosive growth of large scales (the site of localized pairing). A localized subharmonic forcing accelerates and magnifies the result. With global subharmonic forcing, the original defect has practically no dynamical significance since a global vortex pairing is promoted. Examination of the phase portraits for the three cases (not shown), indicates that no defects appear in any of the subharmonic patterns at the site of the original defect. The original defect has not survived the scale transition (pairing). It comes closest to surviving for case III in the following sense. During the first global pairing, the original defect site contains less energy at the subharmonic scale (cf. figures 15*g* and 8*c*). The weakness in amplitude in this region persists and promotes the transition to larger scales farther downstream. The defect which does appear in case III, as mentioned earlier, occurs considerably later in time, and is probably a result of the initial forcing (cf. figure 6*c*). The significant growth in excess energy for case III shown in figure 15(*d*) is thus a combination of the presence of this secondary defect, and the region of subharmonic weakness in the vicinity of the original defect.

Finally, as a means of summarizing the information contained in figures 13–15, an averaged excess energy is defined. A spatial extent for the subharmonic region is set by fixing a threshold value for the excess. Figure 16(*a*–*c*) give the excess energy densities averaged over the regions defined by the thresholds $2\times$, $4\times$, $10\times$.

† If one imagines a broad band of subharmonic disturbances to be unstable, this band is least suppressed by the presence of the fundamental in the vicinity of the defect where the fundamental has the lowest amplitude. The nonlinear suppression mechanism was noted by Coullet, and explored in more detail in Yang (1990), Yang *et al.* (1993).

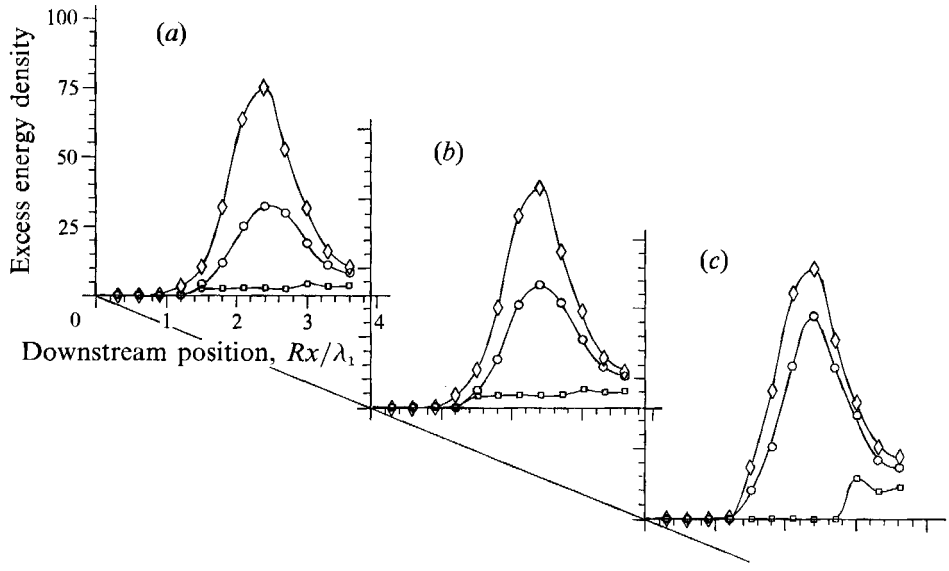

FIGURE 16. Excess energy density as a function of normalized downstream distance: (*a*) threshold = 2; (*b*) threshold = 4; (*c*) threshold = 10. ○, case I; ◇, case II; □, case III.

6. Geometry of the subharmonic 'patches'

6.1. *Patch planform*

The shape or planform of a subharmonic patch containing excess energy density greater than 10× is shown in figure 17. This is case I, and the patch is entirely contained within the measurement domain. It develops a roughly symmetrical planform having a rounded bow and a flat trailing edge. (Remember though, the patch is a space–time image, not a true 2-space image. The vertical coordinate is time the lateral coordinate is space. Also, the scale in figure 17 is distorted – the lateral scale must be multiplied by a factor of 2.9.) For case II, the situation is complicated because the patch reaches the lateral measurement boundaries. The geometry has little meaning in this case, but it is clear that the patch containing subharmonic forcing grows much more rapidly in the spanwise direction.

Numbers representing patch areas are plotted in figure 18 for several thresholds. Planform area is expressed in units of $(T_1 \times \lambda_1)$, and the rates of increase of area reflect the explosiveness of the process. The insert in figure 18 shows patch area for case I – no subharmonic forcing – plotted in log–log coordinates for the three thresholds. Between the beginning of growth and the maximum area location near $Rx/\lambda_1 = 2.5$, the slope is close to two, indicating patch area growing proportional to the square of downstream distance.

6.2. *Relative movement/rate of extension*

The relative locations of the centroids of the growing subharmonic regions with respect to the convected position of the original defect are plotted in figure 19. The centroid is defined as

$$z_c = \sum_i \sum_j z_j \frac{e_{i,j}}{\sum_i \sum_j e_{i,j}}, \tag{31}$$

$$t_c = \sum_i \sum_j t_i \frac{e_{i,j}}{\sum_i \sum_j e_{i,j}}, \tag{32}$$

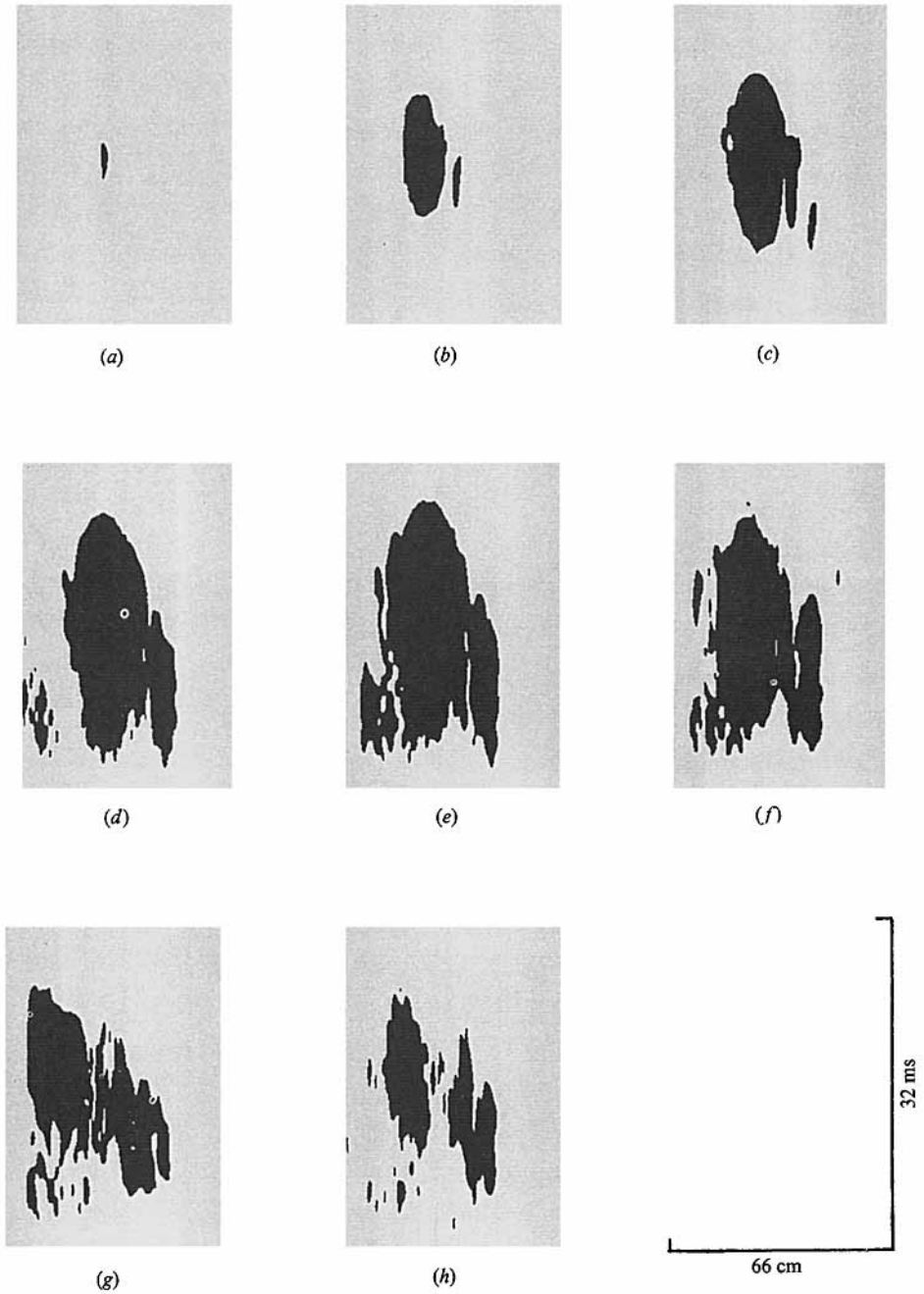

FIGURE 17. Representation of the area with an excess energy density above 10 (case I). The vertical axis is time, the horizontal axis is span. (*a*) $Rx/\lambda_1 = 1.5$; (*b*) $Rx/\lambda_1 = 1.8$; (*c*) $Rx/\lambda_1 = 2.1$; (*d*) $Rx/\lambda_1 = 2.4$; (*e*) $Rx/\lambda_1 = 2.7$; (*f*) $Rx/\lambda_1 = 3.0$; (*g*) $Rx/\lambda_1 = 3.3$; (*h*) $Rx/\lambda_1 = 3.6$.

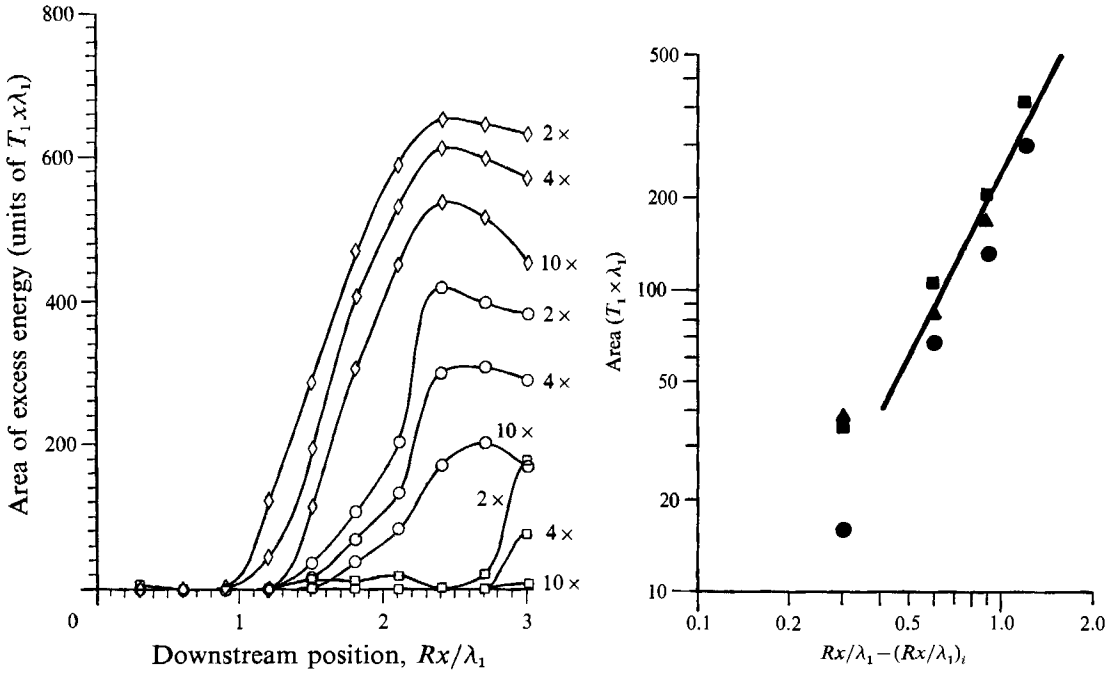

FIGURE 18. Value of the area containing excess energy density above the indicated thresholds 2×, 4×, 10×. ○, case I; ◇, case II; □, case III. Insert shows area versus incremental downstream distance in log coordinates. The line has slope 2. ■, Threshold 2×; ●, 4×; ▲, 10×.

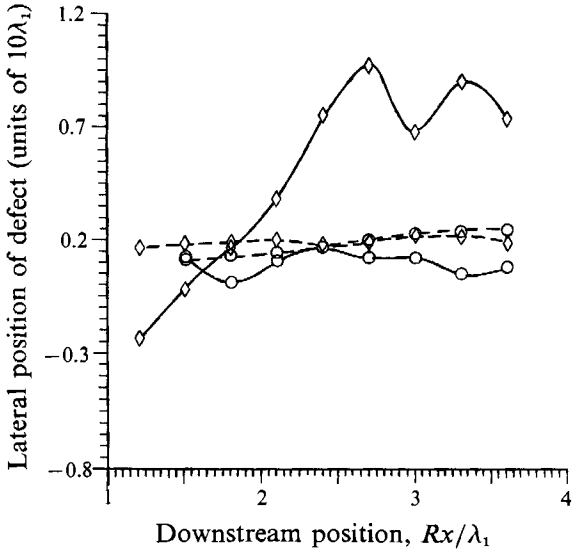

FIGURE 19. Centroid of the area containing excess energy density above 2×. Case I: ○——○——, $t_c - t_{defect}$; ○——○——○, $z_c - z_{defect}$. Case II: ◇——◇——, $t_c - t_{defect}$; ◇——◇——◇, $z_c - z_{defect}$.

with
$$e_{i,j} = \frac{2}{C_g} \int_{2a_1 - \frac{2}{3}a_1}^{4a_1 + \frac{4}{3}a_1} |f_W(a, z_j, t_i)|^2 \frac{da}{a} > \text{threshold} = 2. \tag{33}$$

Since these quantities are weighted by the energy density, they tend to reflect the small central peak within the patch, and are not sensitive to the presence of the lateral boundaries. For as long as the original defect is visible in the pattern, it

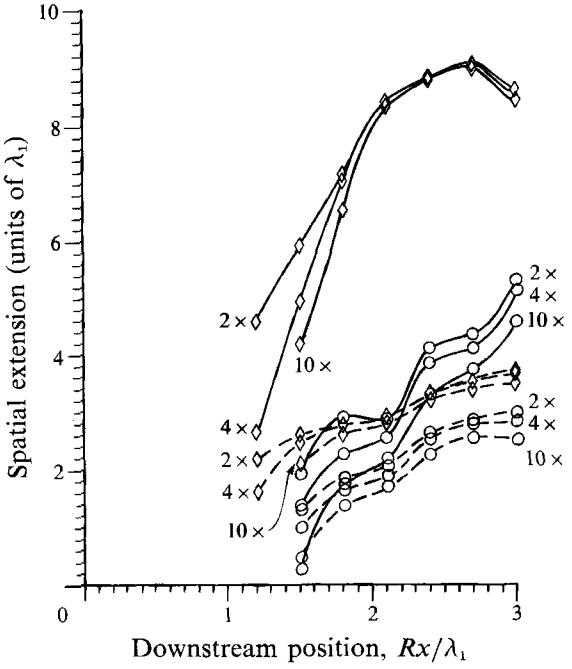

FIGURE 20. Second moments of the centroid of the area containing excess energy density above the indicated thresholds. Case I: ○---○---, t_σ; ○——○——○, z_σ. Case II: ◇---◇---, t_σ; ◇——◇——◇, z_σ.

remains within a wavelength or two of the initial span position and advects downstream with the mean speed $\bar{U}$. This behaviour is assumed throughout. With no subharmonic forcing, the centroid of the patch is initially slightly displaced from the defect, and there is little change farther downstream. For case II, there is much greater lateral motion. The motion is the result of the patch originating in the subharmonic domain to one side of the defect, then moving rapidly toward the peak region visible in figure 14(*c*). This point is approximately eight wavelengths to the right of the original defect.

A measure of the rapidity of growth in the span and time directions can be obtained by estimating the second moments about the centroid. That is

$$z_\sigma = \left[\sum_i \sum_j (z_j - z_c)^2 \frac{e_{i,j}}{\sum_i \sum_j e_{i,j}}\right]^{\frac{1}{2}}, \tag{34}$$

$$t_\sigma = \left[\sum_i \sum_j (t_i - t_c)^2 \frac{e_{i,j}}{\sum_i \sum_j e_{i,j}}\right]^{\frac{1}{2}}, \tag{35}$$

Plots of these two quantities for several thresholds are given in figure 20. The time coordinate has been converted to a space coordinate by multiplication with $\bar{U}$, and the vertical axis is expressed as fractions of the wavelength λ_1. Perhaps the most interesting information is contained in the initial rates of growth in both the longitudinal (time) direction and the span direction obtained from the slopes of the various curves in figure 20. The expressions for rates of growth are

$$\Delta t_\sigma = m_t \lambda_1 \Delta(Rx/\lambda_1) = m_t R \Delta x, \quad \Delta z_\sigma = m_z R \Delta x, \tag{36}$$

	Fundamental pattern (case I)		Pattern with local subharmonic $\frac{1}{2}f_2$ (case II)	
Threshold	Longitudinal extension rate	Spanwise extension rate	Longitudinal extension rate	Spanwise extension rate
2×	0.70	1.06	0.40	2.04
4×	0.78	1.24	0.67	3.10
10×	0.92	1.52	0.58	3.29

TABLE 1. Rates of patch spread, $U_\sigma/\bar{U}$, $W_\sigma/\bar{U}$

where the m are the least-squares linear slopes estimated over the first four downstream stations. The growths in t_σ and z_σ are sensibly linear over this range, and have slopes of approximately $\pm 10\%$ accuracy. Linear growth in t_σ and z_σ again supports the conclusion that patch area $\sim t_\sigma z_\sigma$ grows as the square of downstream distance.

Alternatively, two velocities can be defined:

$$\Delta t_\sigma/\Delta t \equiv U_\sigma = m_t R\,\Delta x/\Delta t, \tag{37}$$

$$\Delta z_\sigma/\Delta t \equiv W_\sigma = m_z R\,\Delta x/\Delta t, \tag{38}$$

giving in the convected frame, $\Delta x/\Delta t = \bar{U}$,

$$U_\sigma/\bar{U} = m_t R, \quad W_\sigma/\bar{U} = m_z R. \tag{39}$$

These velocity ratios are listed in table 1 as a function of threshold and forcing condition. There is a consistent trend for the rates of extension to increase with increasing threshold. But these weighted rates of extension are dominated by the large values of excess energy density near the defect, and are consequently not strong functions of the threshold for the thresholds used.

The ratio of spanwise extension to longitudinal extension is essentially independent of threshold. For the fundamental pattern (case I), the ratio is 1.58 ± 0.08. In effect, the subharmonic region spreads 60% faster in the span direction. The spreading rates (or velocities) are reasonable fractions of the characteristic convection velocity $\bar{U}$. The fact that W_σ is greater than U_σ implies a lack of shape similarity for the growing patch. The patch is preferentially elongating in the spanwise direction, i.e. becoming more two-dimensional. The shape changes may not be so evident in figure 17, but the calculation of the weighted variances t_σ, z_σ should be regarded as the more reliable indicator. The quantity $W_\sigma/\bar{U}$ can also be interpreted as the half-angle for lateral spread of the patch. This angle is approximately $52° \pm 5°$, and depends only weakly on threshold. The largeness of the angle again reflects the explosiveness of the process and the tendency of the resulting structure to become 'two-dimensionalized'.

The spreading patch can be compared with a theoretical linear theory estimate by Balsa (1989). Balsa has determined the linear (Green's function) response to a point force in the vertical direction applied to a region of constant vorticity between two parallel streams. The response is a localized wave packet containing waves near the most unstable wave. Balsa finds the area of the disturbed region to grow $\sim t^2$ in a coordinate system moving with the group velocity (or $\sim x^2$, from some arbitrary fixed origin). The lateral spread, or spanwise extension using our present nomenclature, is predicted to be

$$\Delta z/\Delta x \approx 1.0R.$$

The result is a half-angle prediction of approximately 27° for the lateral spread rate, or about half the measured angular spread rate of our patch. The two physical situations are different, of course, and there is no reason to expect *close* agreement for the two spreading rates. The model linear problem does suggest that relatively large angles for the spreading rate can be anticipated. Yang *et al.* (1992) show that the patch spreading rate can be closely matched by a proper tuning of model equations describing the nonlinear process.

With the imposition of subharmonic scales locally, the rate of spread in the span direction is just about doubled, while the longitudinal extension rate is decreased by about 30%. The ratio W_σ/U_σ is considerably increased to 5.1 ± 0.5.

7. Concluding remarks

The most important conclusions to come from the present study relate to the relative dominance of two-dimensional and three-dimensional aspects of the flow. The defects, which arise naturally in the flow, serve as nuclei for further change. Pairing is first initiated here, and results in a broadband transition to larger scales. The size of the affected region grows more rapidly in the span direction than in the stream direction, thus preserving a certain tendency toward two-dimensionality. To gain an appreciation of the significance of the rates of area increase shown in figure 18, the following example is given. In a downstream distance $R\Delta x/\lambda_1 \approx 2.5$, which is characteristic of the generally accepted distance required to complete the pairing interaction, the area of the patch with excess energy $10\times$ (case I) has grown from zero to about 200 $(T_1' \times \lambda_1)$. If defects were randomly sprinkled in time throughout the mixing-layer span at the plate trailing edge, an initial average density of 5×10^{-3} in $(T_1' \times \lambda_1)$ would be sufficient to fill the planform with paired vortices in the same downstream interval $(R\Delta x/\lambda_1 = 2.5)$. Since the measured initial density of defects is $1\text{–}2 \times 10^{-2}$ in $(T_1' \times \lambda_1)$ (Browand & Prost-Domasky 1990), the mechanism of large-scale growth at defect sites seems rapid enough to account for the pairing transition in its entirety. Figure 21 is a crude planform portrayal of how the process might be imagined to function as pairing is initiated at many sites along the span. Here we have converted the measured z-t images into z-x images. This is not correct in detail, but by estimating the z-t-x envelope containing the patch, we were able to convince ourselves that the qualitative planform shape in z-x would be similar to the z-t observations. The original defect is observed to disappear once the subharmonic transition takes place, but additional defects can be expected at the boundaries of patches arising from competing sites. Thus the process is envisioned to continue through a succession of generations.

Forcing locally at the subharmonic frequency $\frac{1}{2}f_2$ accentuates the three-dimensionality of the patch growth process by significantly increasing the excess energy density, but it also hastens the completion of the process by increasing the lateral spreading rate. Forcing globally at the subharmonic frequencies $\frac{1}{2}f_1$ and $\frac{1}{2}f_2$ renders the original defect ineffective. In fact global subharmonic forcing creates in the region of the defect a diminished subharmonic amplitude, which in the succeeding generation behaves as if it were a defect. In addition, several generations of defects can be introduced by the initial forcing. This apparently happened inadvertently for the case of global subharmonic forcing.

It remains to discuss how these results might be integrated with what is presently understood about the large-scale dynamics (pairing) in mixing layers. Pairing has traditionally been viewed as a two-dimensional, or more appropriately a quasi-two-

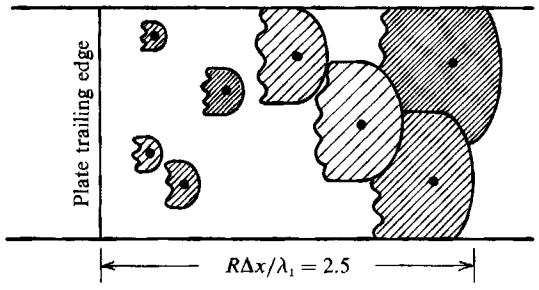

FIGURE 21. Planform sketch of mixing layer illustrating patches growing from numerous defect sites to fill the surface. Not to scale.

dimensional, process. The term quasi-two-dimensional is taken to mean that the physical mechanism is a two-dimensional one. Of course, for naturally developing (unforced) mixing layers, pairing interactions are always three-dimensional, but no three-dimensionality need be involved to understand the process. Pierrehumbert & Widnall (1982) demonstrated mathematically that the subharmonic instability of a row of Stuart vortices was maximized for two-dimensional disturbances. They also showed that typical amplification rates for three-dimensional modes were only slightly smaller for wave vector angles less than about 45°. Thus the instability is broadband with regard to the orientation of the subharmonic disturbance. Disturbance e-folding distance, Rx/λ_1, was of the order of unity, resulting in a rapid growth of any initial, imposed perturbation. The two facts together suggest that there are many transition scenarios depending upon the relative magnitudes of two- and three-dimensional initial disturbances. The experimental work of Lasheras, Cho & Maxworthy (1986), Lasheras & Choi (1988), and the numerical experiments of Corcos & Lin (1984) lend support to the multiple scenario viewpoint. Rogers & Moser (1992) and Moser & Rogers (1993) have recently discussed several scenarios in great detail utilizing direct numerical simulation (DNS).

To these multiple scenarios, we have added an additional one, which is inherently three-dimensional. It is the amplification of a broad band of larger scales in the vicinity of a defect in the pattern of the fundamental. It may be likened, as Williamson (1992) suggests in a related context, to the development of a turbulent spot in a laminar boundry layer. In describing boundary-layer transition, distinction is often made between routes stemming from an organized wave field – Tollmien–Schlicting waves and subharmonics – and the route described by the confluence of disturbances arising from isolated turbulent spots. The same distinction may be appropriate for unbounded shear flows, although the analogy is not perfect.

The estimate in the first paragraph above has shown that pairing arising from pattern defects is sufficiently rapid to account completely for the transition to larger scales. But pairing also takes place in the absence of such isolated nucleii. 'Natural transition' can be expected to depend upon both processes. It is probably impossible to describe natural transition without a proper characterization of the initial disturbance field.

None of the existing direct numerical simulations of mixing layers have detected the three-dimensional structure described here. This is understandable. In almost all calculations, initial conditions are composed of a combination of two-dimensional modes and spanwise periodic three-dimensional modes. Such initial conditions exclude the possibility of pattern defects. It would be interesting to introduce defect structure as an initial condition, and to follow the downstream evolution numerically.

The wavelet transform has proved to be a useful tool for quantifying the localized transition. But a physical understanding is still incomplete. We do not know, for example, how vortex lines link up within the expanding subharmonic region. Nor do we understand the precise mechanism of spreading. In a companion project, Yang *et al.* (1993) have compared 2-space+time numerical calculations, based upon a nonlinear evolution equation model, with some of the data presented here. (The vertical coordinate is suppressed in the simulations, making them simpler than DNS solutions.) Qualitatively, the behaviour near defect locations appears strikingly similar to the experiment. These comparisons provide physical insight, and the hope of a useful predictive capability for shear flows which respond strongly to small levels of forcing. In the future, such intercomparisons must focus on quantitative details.

Features like those described here have been observed by other researchers, for example by Nygaard & Glezer (1991). Similar features also arise in other, related geometries, the most notable to date being the cylinder wake at lower Reynolds numbers, as in Provensal, Mathis & Boyer (1987), Van Atta & Gharib (1987), Van Atta & Piccirillo (1990), Piccirillo & Van Atta (1993), Eisenlohr & Eckelmann (1989), Lewis & Gharib (1992), and Williamson (1989, 1992). Williamson (1992), in an elegant experiment, demonstrates that the presence of a small localized ring, placed upon an otherwise two-dimensional cylinder at Reynolds numbers of about 200, generates defects in the downstream vortex structure. Each defect region grows into a large-scale Λ-structure encompassing many shed vortices. The spread of the Λ-structure is likened to the growth of a turbulent spot in a laminar boundary layer. At Reynolds numbers exceeding 280, Λ-structures form throughout the span of the flow spontaneously, without the need for the small ring. It is hoped that a more explicit connection can be provided between these various experiments.

A related issue is the presence of increased levels of small-scale turbulent activity in the vicinity of defects. The present experiment was not meant to explore the production of small scales, but the work of Williamson (1992), of Nygaard & Glezer (1991), and of Ho *et al.* (1991), demonstrate important linkages between large-scale behaviour and small-scale fluctuations. These linkages could be strengthened by additional experimental work.

This work was supported by ONR Fluid Mechanics Program, under the University Research Initiative. We are indebted to S. Legendre and P. Taniguchi, who were responsible for collecting the bulk of the data discussed here. We are particularly indebted to G. R. Spedding. Not only was he instrumental in formulating the 2-D wavelet transform used, but his expertise was utilized repeatedly in the formatting, processing, and plotting of data.

REFERENCES

Balsa, T. F. 1989 Three-dimensional wave packets and instability waves in free shear layers and their receptivity. *J. Fluid Mech.* **201**, 77–97.

Berry, M. 1980 Singularities in waves and rays. In *Les Houches - Physics of Defects*, pp. 453–541.

Browand, F. K. 1986 The structure of the turbulent mixing layer. *Physica* **D18**, 135–148.

Browand, F. K. & Ho, C.-M. 1987 Forced, unbounded shear flows. *Nucl. Phys.* **B2**, 139–158.

Browand, F. K. & Prost-Domasky, S. 1990 Experiment on pattern evolution in the 2-D mixing layer. In *New Trends in Nonlinear Dynamics and Patterning Phenomena: The Geometry of Non Equilibrium* (ed. P. Coullet & P. Huerre). Plenum.

Browand, F. K. & Troutt, T. R. 1980 A note on spanwise structure in the two-dimensional mixing layer. *J. Fluid Mech.* **97**, 771–781.

CHANDRSUDA, C., MEHTA, R. D., WEIR, A. D. & BRADSHAW, P. 1978 Effect of free stream turbulence on large structure in turbulent mixing layers. *J. Fluid Mech.* **85**, 693–704.

CORCOS, G. M. & LIN, S. J. 1984 The mixing layer: deterministic models of a turbulent flow. Part 2. The origin of the three-dimensional motion. *J. Fluid Mech.* **139**, 67–95.

COULLET, P., GIL, L. & LEGA, J. 1989 A form of turbulence associated with defects. *Physica* D **37**, 91–103.

DALLARD, T. & SPEDDING, G. R. 1992 2-D wavelet transforms: generalisation of the Hardy space and application to experimental studies. *Eur. J. Mech.* B/*Fluids* (in press).

EISENLOHR, H. & ECKELMANN, H. 1989 Vortex splitting and its consequences in the vortex street wake of cylinders at low Reynolds numbers. *Phys. Fluids* A **1**, 189.

FARGE, M. 1992 Wavelet transforms and their applications to turbulence. *Ann. Rev. Fluid Mech.* **24**, 395–457.

FARGE, M., GUEZENNEC, Y., HO, C.-M. & MENEVEAU, C. 1990 Continuous wavelet analysis of coherent structures. In *Center for Turbulence Research, Proc. 1990 Summer Program*, pp. 331–348.

GROSSMAN, A. & MORLET, J. 1984 Decomposition of Hardy functions into square integrable wavelets of constant shape. *SIAM J. Math. Anal.* **15**, 723–736.

HO, C.-M., ZOHAR, Y., FOSS, J. K. & BUELL, J. C. 1991 Phase decorrelation of coherent structures in a free shear layer. *J. Fluid Mech.* **230**, 319–337.

LASHERAS, J. C., CHO, J. S. & MAXWORTHY, T. 1986 On the origin and evolution of streamwise vortical structures in a plane free shear-layer. *J. Fluid Mech.* **172**, 231–258.

LASHERAS, J. C. & CHOI, H. 1988 Three-dimensional instability of a plane free shear layer: an experimental study of the formation and evolution of streamwise vortices. *J. Fluid Mech.* **189**, 53–86.

LEWIS, C. G. & GHARIB, M. 1992 An exploration of the wake three dimensionalities caused by a local discontinuity in cylinder diameter. *Phys. Fluids* A **4**, 104–117.

MALLAT, S. G. 1989 Multifrequency decompositions of images and wavelet models. *IEEE Trans. Acoust. Speech Signal Proc.* **37**, 2091–2110.

MONKEWITZ, P. A. 1988 Subharmonic resonance, pairing and shredding in the mixing layer. *J. Fluid Mech.* **188**, 223–252.

MOSER, R. D. & ROGERS, M. M. 1993 The three-dimensional evolution of a plane mixing layer: pairing and transition to turbulence. *J. Fluid Mech.* **247**, 275–320.

NYGAARD, K. J. & GLEZER, A. 1991 Evolution of streamwise vortices and generation of small-scale motion in a plane mixing layer. *J. Fluid Mech.* **231**, 257–301.

PICCIRILLO, P. S. & VAN ATTA, C. W. 1993 An experimental study of vortex shedding behind linearly tapered cylinders at low Reynolds numbers. *J. Fluid Mech.* **246**, 163–195.

PIERREHUMBERT, R. T. & WIDNALL, S. E. 1982 The two- and three-dimensional instabilities of a spatially periodic shear layer. *J. Fluid Mech.* **114**, 59–82.

PROVENSAL, M., MATHIS, C. & BOYER, L. 1987 Bénard–von Kármán instability: transient and forced regimes. *J. Fluid Mech.* **182**, 1–22.

ROGERS, M. M. & MOSER, R. D. 1992 The three-dimensional evolution of a plane mixing layer: the Kelvin–Helmholtz rollup. *J. Fluid Mech.* **243**, 183–226.

SPEDDING, G. R., DALLARD, T. & BROWAND, F. K. 1991 The design and application of 2-D wavelet transforms for fluid turbulence data. In *Proc. DARPA/ONERA Workshop on: Wavelets and Turbulence, Princeton University.*

VAN ATTA, C. & GHARIB, M. 1987 Ordered and chaotic vortex streets behind circular cylinders at low Reynolds numbers. *J. Fluid Mech.* **174**, 113–133.

VAN ATTA, C. W. & PICCIRILLO, P. 1990 Topological defects in vortex streets behind tapered circular cylinders at low Reynolds numbers. In *New Trends in Nonlinear Dynamics and Pattern-Forming Phenomena* (ed. P. Coullet & P. Huerre), pp. 243–250. Plenum.

WILLIAMSON, C. H. K. 1989 Oblique and parallel modes of vortex shedding in the wake of a circular cylinder at low Reynolds numbers. *J. Fluid Mech.* **206**, 579–627.

WILLIAMSON, C. H. K. 1992 The natural and forced formation of spot-like 'vortex dislocations' in the transition of a wake. *J. Fluid Mech.* **243**, 393–441.

YANG, R. 1990 Two-dimensional models of pattern formation in free shear flows. Ph.D. thesis, Univ. of S. Calif. – Dept. of Aerospace Eng. Los Angeles.

YANG, R., BROWAND, F. K., COULLET, P. & HUERRE, P. 1993 A model of defect-induced pairing in mixing layers. *J. Fluid Mech.* **248**, 403–423.